Flight Testing Of Power Kites

Bachelor Thesis

By

ICÍAR MARTÍN MEJÍAS

Tutored and Supervised by

GONZALO SÁNCHEZ ARRIAGA

UNIVERSIDAD CARLOS III DE MADRID
SCHOOL OF ENGINEERING
DEPARTMENT OF BIOENGINEERING AND AEROSPACE ENGINEERING

SEPTEMBER 2017

ABSTRACT

Advent emerging economies and the constant world population growth lead to think of alternatives to fossil fuels to generate usable power. These sources of energy are not only harmful to the environment but finite, and they are about to be exhausted. Airborne Wind Energy (AWE) is a new way to produce clean energy that promises to be more efficient than current renewable sources. Its aim is to harvest the energy of the stable and stronger winds in the upper layers of the atmosphere, which are unreachable for the conventional wind turbines used nowadays.

There are several companies and institutions currently working on the development of this type of energy, being Universidad Carlos III de Madrid one of them. This university is developing an AWE system composed of two kite-surf kites connected to a control bar by means of several tethers. The objective of this thesis is to contribute to this research characterizing these kites with a CAD software and designing, implementing and testing a weather station which is able to measure the wind velocity (its magnitude and heading). Results will be used on the one hand to validate a Matlab simulator of the kites and on the other hand to make progress in the future flight test campaigns.

Keywords: Airborne Wind Energy, kites, wind velocity, weather station, airspeed, wind direction, flight test.

DEDICATION AND ACKNOWLEDGEMENTS

First of all, I would like to dedicate this thesis to my parents, who have always supported me either in good or tough moments. Thank you for your dedication and the big effort you do to provide me and my sister with the best education. What I am nowadays is in large part what I have learnt from you.

Thank you to all my friends and colleagues for encouraging me at all times, for having gone together all these years. I am really fortunate to count on you. May our ways take us to new adventures together.

Especial thanks to two important people whose support and nature have been my pillars through all this way, Sergio and my sister Andrea. Thank you for your time and for making me happy everyday, for sharing with me incredible moments that give meaning to life.

On the other hand, I would like to thank my tutor and supervisor Gonzalo Sánchez Arriaga and to Ricardo Borobia, for supporting and advising me during the course of this project. Thanks also to some people at UC3M that helped me with technical issues when I needed, especially Carlos Sanmiguel, Carlos Cobos and Alejandro Güemes.

Finally, thanks to those people from which I learned something in my life or have inspired me in some way. And to those who fight everyday to make the world a better place especially in these difficult moments.

Vires Acquirit Eundo,

Icíar

AUTHOR'S DECLARATION

I hereby declare that I have formed, completed and written the Bachelor Thesis named "Flight Testing Of Power Kites". The contents of the present dissertation are original unless those in which the reference is specified next to them.

Icíar Martín Mejías
Madrid, September 2017.

TABLE OF CONTENTS

LIST OF TABLES

TABLE **Page**

List of Figures

CHAPTER 1

INTRODUCTION

This first chapter is devoted to acquaint the reader with the Airborne Wind Energy (AWE) field, its background, principles and availability. On the other hand, the objectives and methodology of this thesis will be exposed, as well as the motivation to develop it.

1.1 Motivation

"If Earth's history is compared to a calendar year, modern human life has existed for 23 minutes and we have used one third of Earth's natural resources in the last 0.2 seconds" [28]. This is the reality the humanity faces nowadays. With the advent of emerging economies, and the continuous increase of population the energy demand has increased in the last years and continues growing everyday. Currently, humanity consumes around 17 Terawatts of power [28, 69] and more than the 85% are provided by fossil fuels: oil, coal and natural gas (Figure 1.1), according to the World Energy Council 2016 [46]. This is a huge amount of power that we actually cannot afford due to two main reasons:

1. The Earth's energy demand is continuously increasing, and there are no physical resources to sustain the world's power consumption in the close future using fossil fuels as the main source of energy. The U.S Energy Information Administration predicts that the world energy consumption will increase by 56% between 2010 and 2040 [8]. And fossil fuels are not infinite. According to the last BP Statistical Review of World Energy [49], estimated proved reserves of coal would be exhausted in 2169, natural gas in 2068, and the entirety of crude oil reserves in 2066.

2. Due to the abusive use of fossil fuels, human action is having a crucial irreversible impact on the environment. Some of the immediate concerns affecting it now are:

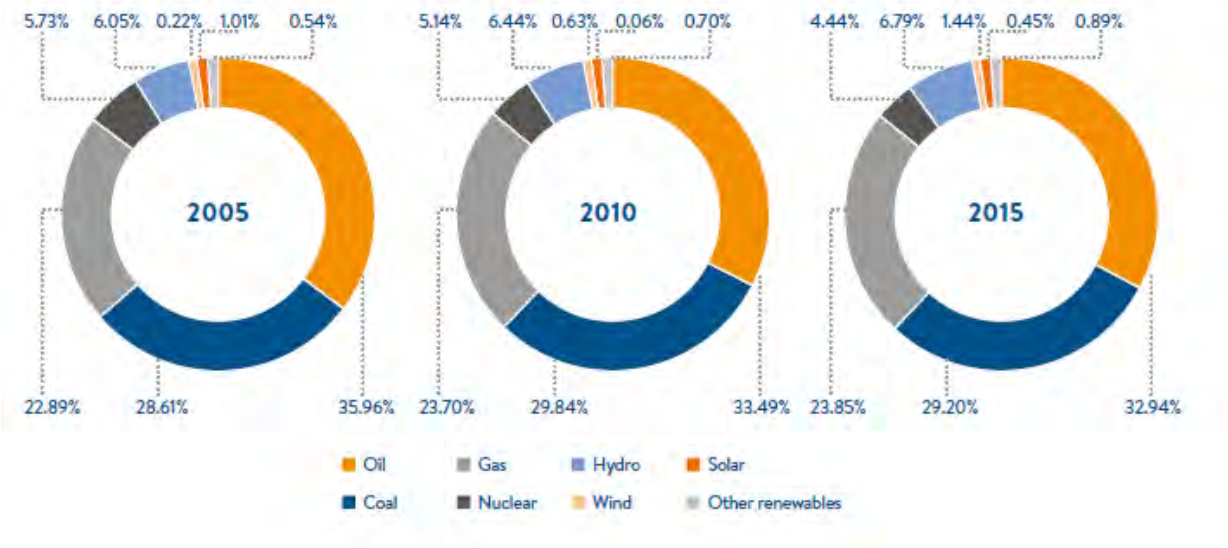

FIGURE 1.1. Comparative of primary energy consumption over the past 15 years [46]

.

- **Rising world temperatures** due to the induced greenhouse effect, largely caused by the burning of fossil fuels that release huge amounts of carbon dioxide to the atmosphere. This feature can be observed in [33], an interactive graph with the global temperature rise on the Earth's surface over the past years. The year 2016 ranks as the warmest on record. Moreover, recent studies have shown that even if human-caused emissions of carbon dioxide stopped now, they would still affect global warming for more than 1,000 years [45].

- **Melting ice caps and rising sea levels**. Due to the global temperature rise, the ice caps are getting melted. Antarctica's level of ice has been reduced 9 meters height the last five years [68], and the Arctic has lost one third of its ice since the 1970s. Of course all this amount of melted ice increases the sea level. According to NASA, the sea level has been rising continuously during the last decades (Figure 1.2); and this fact is having severe consequences. Such is the case that several Pacific islands have been already covered by water, and many world cities which are located directly in flood plain areas may lost part of their territories due to the same reason. As an interesting data, it is estimated that climate change could allow ships to cross the North Pole by 2040 [68]. Another example of the impact of the sea level rise which is currently happening is the intensification of the 'King tides' which usually flood Florida.

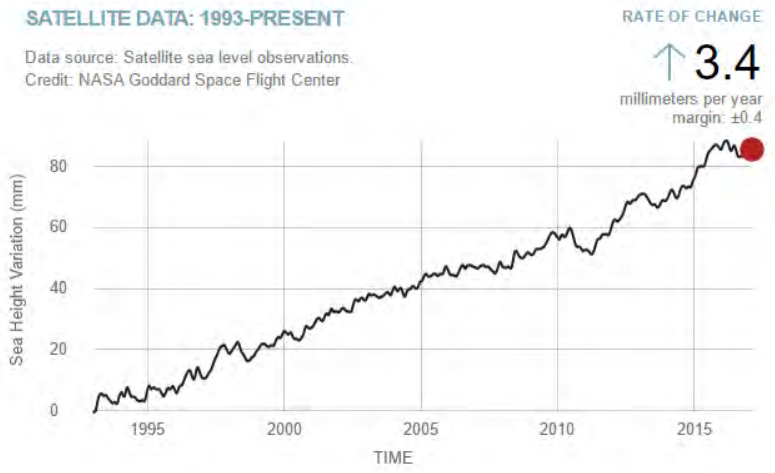

FIGURE 1.2. Evolution of sea rising level in the last decades [34]

.

- **Extreme weather conditions**. The effects of climate change are thought to increase the severity of several natural events such as hurricanes, monsoons, floods, droughts and heatwaves. And it seems to be caused greatly by the fast melting Arctic, which is affecting weather patterns in the whole planet. A proof of the impact of the human 'fingerprint' on the weather conditions is that the east Mediterranean zone is recently suffering the worst droughts of the last 900 years.
- **Changing eco-systems**. Several scientific studies show that climate change is inducing changes in natural habitats due to the rising temperatures, extreme weather conditions and sea levels. It is supposed that coastal habitats may disappear in the close future and therefore their inhabitants. One clear example of the devastating effect of the extreme changes in the climate is the disappearance of the 50% of the world's coral reefs in the last 30 years [68]. This cipher is estimated to be increased up to 90% by 2050 [42]. On the other hand many species such as koalas, different types of birds, sea turtles or Antarctic penguins are also threatened and could be extinct before the end of this century.

These concerns could be mitigated if the world's energy demand could be satisfied using other resources than fossil fuels. It means, if renewable energies would be able to provide sufficient power at an economic cost. In the last decade, this type of energies have increased their contribution to world's power supply, as it can be observed in Figure 1.1, being the hydropower the leading renewable source of electricity generation globally (71% of total renewable electricity). However, in comparison to fossil fuels and nuclear energy, renewable sources are currently out of the energy market. The first generation of this type of energy has not been efficient enough in order to compete with the leaders. There are several reasons to explain this fact, but

principally it has occurred due to the high cost of the energy production (and especially the initial infrastructure investment) that renewable energies have had (and still have). Therefore it may be time to invest in other types of renewable energies that may deliver more power at a lower cost. And this can be case of the Airborne Wind Energy, which is the topic of this thesis. This new concept of harvesting wind power is intended to ameliorate the performance of renewable energies, especially of conventional wind energy coming from wind turbines. Therefore several comparisons will be made with respect to this source of power.

1.2 Principles of Airborne Wind Energy

In spite of the fact that AWE is currently emerging, there exists a wide variety of systems already patented. AWE systems can be classified attending to several aspects. The most notable one is the way of producing electric power. An AWE system is an airborne device that converts the kinetic energy of the wind into usable electric power. It means, it transforms mechanical energy into electric energy. This transformation can be done in two different ways. The first option is to transfer the mechanical energy of the wind generating traction on a mechanical tether connected to a generator located on ground. This is the so-called Ground-gen AWE (GG-AWE). In this case, a light device such as a kite or a simple aircraft moves in the air describing a selected path. It is connected to a tether that reels in and out that is in turn attached to a generator that allows the power production. On the other hand, the electric power can be generated directly on the aircraft by using a turbine located on-board. Then, the electric power is transferred to the ground station by means of electrical tethers (wires). This is the Fly-gen type (FG-AWE). Figure 1.3 shows both possibilities.

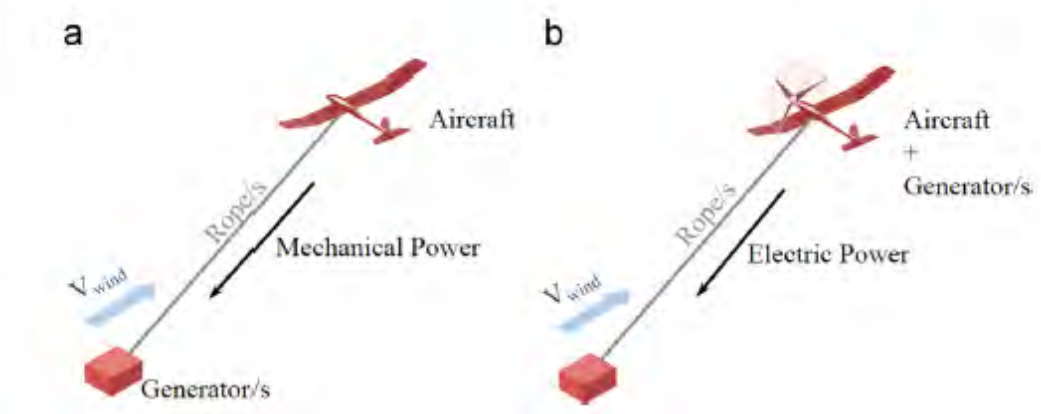

FIGURE 1.3. Different ways of generating electric power in AWE systems. Ground-gen (a) vs Fly-gen (b). Figure from [44].

Compared to the traditional wind power generation, the kite or aircraft of an AWE system represents the fastest moving part of a large wind turbine (the tips of the rotor blades), since

it seems that the outer and much more thinner and lighter 30% of the blades of a traditional wind turbine provides more than half of the total power [36]. The detailed explanation about the functioning of AWE devices as well as about the different types of systems involved in this kind of power generation can be found in Chapter 2.

1.2.1 Wind Power Fundamentals

As it has been mentioned, the purpose of AWE devices is to extract kinetic energy from the air stream in order to convert it into usable electrical power. It means, an AWE system has to effectively harvest the power present in the wind. Wind speed (v_w) is therefore a paramount aspect regarding the efficiency and use of this kind of power generation, since the kinetic energy of the wind is given by [37]:

$$E_k = \frac{1}{2} m v_w^2 \tag{1.1}$$

where m is the mass of each air parcel going through the area swept by the blades (in the case of a conventional turbine). Considering a volume of air:

$$V = v_w A \Delta t \tag{1.2}$$

given by the area swept by the blades (a much more useful parameter than the mass) times the distance covered by the wind in a time interval Δt, the mass in Eq. 1.1 can be defined as:

$$m = \rho A v_w \Delta t \tag{1.3}$$

Dividing the kinetic energy over the defined time interval Δt, the power available in the wind turns into:

$$P = \frac{1}{2} \rho A v_w^3 \tag{1.4}$$

It is shown that the power in the wind is proportional to the cube of the air speed. Therefore, this is the main parameter to take into account. It is also proved that wind speed generally increases with height [38], so the higher the turbine is (in this case), the more power it generates. However conventional turbines are not able to reach heights greater than approximately 150 m in general, so the amount of power that they can deliver is quite limited. On the other hand, AWE systems are intended to fly beyond these limits allowing to reach much more higher layers in the atmosphere in order to take advantage of the speed of the wind in these layers, and therefore to generate more power.

As shown in Eq. 1.4, the power available in the wind is a function of the area of the blades for a conventional wind turbine. In the case of AWE systems, in which the area is maybe more difficult to estimate another variable is more useful. This is the power density, given by Eq. 1.5.

This parameter actually accounts for the most important variables affecting power generation, which are the wind speed and the air density.

$$\delta = \frac{P}{A} = \frac{1}{2}\rho v_w^3 \tag{1.5}$$

1.2.2 Crosswind power

The concept of power generation using kites harvesting crosswind was already studied in the 1970's and 1980's by the American engineer Miles Loyd. He investigated and patented the idea of a flying tethered aircraft or kite connected to ground, describing circular paths in the air, and computed the ideal power generated either using ground or fly generation. This is what he called *crosswind kite power*, since the aircraft or kite flies in a crosswind direction. The maximum power estimated by Loyd for a tethered airfoil operated in crosswind under idealized assumptions was given by [47]:

$$P_{max} = \frac{2}{27}\rho A v_w^3 C_L \left(\frac{C_L}{C_D}\right)^2 \tag{1.6}$$

where A is the area of the wing, C_L and C_D the lift and drag coefficients, and v_w the wind speed. Theoretically, a modern wing with a $C_L = 1$, a total $C_D = 0.07$ and a wind of $v_w = 13 m/s$ would generate a power density of 40 kW/m^2 of wing area, which seems to be realistic according to the currently state of the art.

This power density is actually more than 150 times the highest power density of solar irradiation on the earth (1.3 kW/m^2). Therefore the power generated by 1 m^2 of wing of an AWE system is more than 150 times the one generated by a solar panel of the same area at maximum irradiation [47]. In [47] there is an interesting comparison with wind turbines. It seems like if a reinforced wing of an Airbus A380 (845 m^2) was tethered like an AWE device, it could produce a theoretical output of 34 MW assuming that it flew at 500 m altitude. To be conservative this amount could be reduced to 30 MW. This is the power produced by four of the largest existing conventional wind turbines, the Enercon E-126 of 7.5 MW rated power. Adding the mass of the whole turbines (blades and tower) the resultant is more than 300 times the weight of the airborne part of the AWE system formed by the A380 wing. This is a very impacting data that shows how big the save in material would be if AWE systems could substitute conventional turbines delivering the same power. However, it is worth mentioning that Loyd's estimation is computed under ideal conditions, so some limitations have to be added in order to estimate the real power delivered by an AWE device. For example in fly-gen the small turbine onboard would generate some extra drag that reduced the power output.

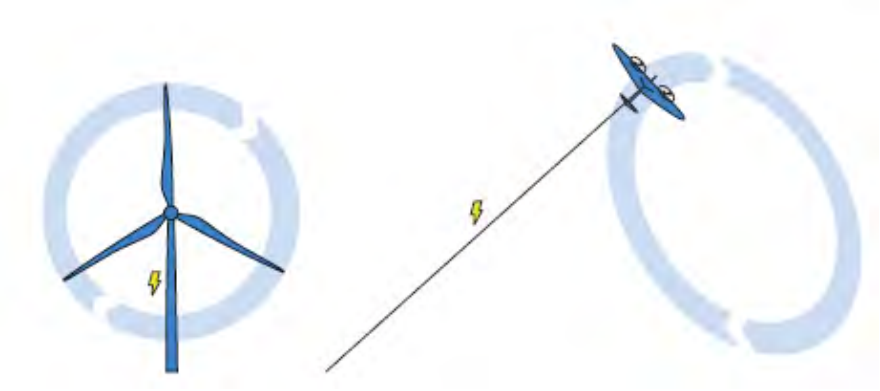

FIGURE 1.4. Airborne Wind Energy System vs traditional wind turbine [47]

.

Regarding the efficiency of an AWE system, it may be estimated using the power harvesting factor ζ, defined as [47]:

$$\zeta = \frac{P_{useful}}{P} = \frac{P_{useful}}{\frac{1}{2}\rho A v_w^3} \tag{1.7}$$

which compares the useful power produced by an AWE system with wing area A with the wind power that flows through a cross sectional area of the same size. The best experimentally realized harvesting factor so far is ζ = 8 as reported by the company Makani Power. Modern wind turbines have a zeta factor of approximately 5.5 [47].

1.2.3 Wind in the atmosphere

AWE devices are intended to reach higher altitudes than conventional wind turbines, where the wind is more stable and strong. This section is devoted to acquaint the reader with a brief explanation on how the wind behaves in the different layers of the atmosphere and which would be the optimal height for AWE systems to operate.
The atmospheric dynamics and thermodynamics are governed by four equations: continuity, thermodynamic, momentum and state equations. It was shown that the wind power available in the atmosphere increases with the cube of the wind speed. Therefore, the most useful equation for AWE applications can be the momentum equation or equation of motion, since it is related to the rate of change of the wind vector. In a rotating reference frame such as the Earth, this equation is defined as [37]:

$$\begin{aligned}
\frac{\partial \mathbf{v_w}}{\partial t} + (\mathbf{v_w} \cdot \nabla)\mathbf{v_w} = & -\frac{1}{\rho}\nabla p && \text{Pressure Gradient} \\
& -2\Omega \times \mathbf{v_w} && \text{Coriolis} \\
& -g\mathbf{k} && \text{Gravity} \\
& +\frac{1}{\rho}(\nabla \cdot \rho \tilde{K} \nabla)\mathbf{v_w} && \text{Turbulence Flux Divergence} \\
& +\frac{\mu}{\rho}\nabla^2 \mathbf{v_w} && \text{Viscous Diffusion}
\end{aligned}$$

where:

- Ω is the Earth's angular velocity
- $\vec{k}$ is the unit vector in z direction
- μ is the dynamic viscosity
- $\tilde{K}$ is the eddy viscosity tensor

This equation is derived from the Newton's second law of motion. The right hand side of the momentum equation is divided in five terms:

1. Pressure gradient force (PGF), which pushes the air from high to low pressure regions (that is the reason of the minus sign). The PGF is perpendicular to the isobars or lines of constant pressure.
2. Coriolis force, which appears due to the rotation of the Earth. It is zero in the Equator and increases towards the Poles.
3. Gravity, which is assumed to be constant with latitude and longitude.
4. Turbulent flux divergence, which is the term representing the eddies effect.
5. Viscous diffusion, which represents viscosity effects.

These terms have more or less influence depending on the altitude of the layers in the atmosphere, and the behaviour of the winds is quite different depending on the terms of the momentum equation that govern them. Therefore a distinction between winds in the upper atmosphere (or high winds) and winds in the lower atmosphere (or low winds) can be made.

High winds in the upper atmosphere, above the boundary layer, are governed by pressure gradient force and Coriolis effects. On the contrary, low winds near the Earth's surface (typically below 500 m) are affected by turbulent and frictional effects inside the boundary layer. Thus these winds are governed by turbulence flux and viscosity diffusion terms.

AWE systems are thought to be able to fly either inside the boundary layer or above it. The most efficient height for this devices to operate would be the lowest as possible where the wind speed was the highest, in order to reduce the drag effect due to the tether. It seems that very

strong winds occur in the jet streams, generally located between 7 and 16 km of altitude. In each hemisphere two different jet streams can be found: the polar jet stream, over mid-latitudes of 7 to 12 km, and a weaker sub-tropical stream found near 30 degrees north and south the Equator. This last stream happens to be at 10-16 km. It is interesting to mention that wind energy available in jet streams is approximately 100 times the global energy demand [38]. However, due to the seasonal nature of this jets, winds are not very stable so it would not be worth placing the AWE devices here. Furthermore, these jet streams are located at too high altitudes and this means a huge penalty due to the tether drag.

According to [38], in which an study of wind power availability worldwide has been made taking data during 27 years, the highest wind power densities are found at altitudes between 8 and 10 km above ground. So, it seems that 10 km is the limit height that is worth exploring for AWE technologies. The same research affirms that power density slightly decreases from 500 m to 2 km altitude, and from here it starts to increase monotonically. Also, from 80 to 500 m, a significant increase in power density has been found. Therefore, it seems that it is not worth placing the device beyond 500m if the altitude is not going to be higher than 2 km.

Most locations on Earth have significant power production potential, although there are regions more prone to be subjected to strong winds. Figure 1.5 shows the optimal height and power density worldwide. Since this data is based on statistical results, percentiles are used to show the optimal values that were exceeded 50%, 68% and 95% of the time during years 1979-2006. It seems that the optimal height is lower than 6 km the 95% of the time worldwide. And the optimal wind power density is greater than 0.2 kW/m^2 the same percentile.

Researchers of [39] have defined a temporally consistent, jet-like vertical wind profiles below 3 km. These profiles are known as *wind speed maxima* (WSM). It seems that they are present in low-level jets (LLJs), which are kind of jet streams in lowest layers of the atmosphere than the polar and the sub-tropical streams. According to their research, these streams could be the key for the maximum exploitation of AWE systems. On the one hand, WSM have stronger wind speeds than the surrounding environment but at altitudes that are not reachable for conventional wind turbines. On the other hand, AWE systems are thought to adapt their attitudes during flight in order to coincide with the WSM core where the speed is highest and turbulence is negligible. Wind power densities are generally high in WSM, exceeding 1 kW/m^2 at most locations. WSM near the polar regions seem to have the highest wind power densities (peaks exceeding 12 kW/m^2), but their location makes them no practical.

1.2.4 Advantages of Airborne Wind Energy

Taking into account all the aspects mentioned about AWE, the systems that used this kind of generation would present the following advantages:

1. Winds are caused mainly by atmospheric pressure differences, and these differences are always present. Therefore, in principle wind power is one of the few renewable energy

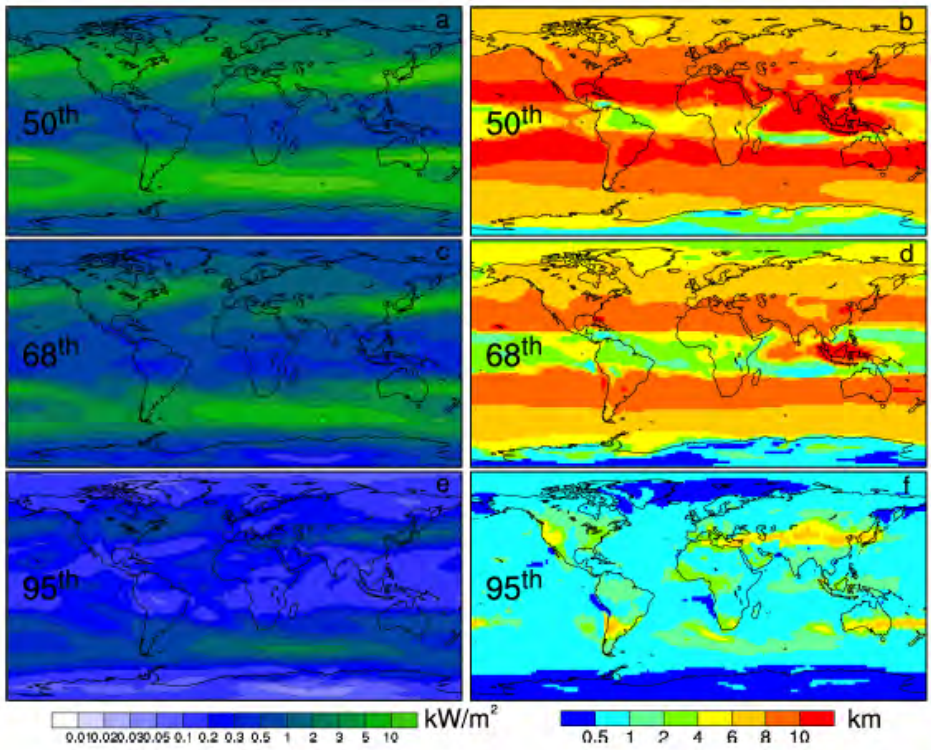

FIGURE 1.5. Optimal wind power density (left) and optimal height (right) that was exceeded 50%, 68%, and 95% of the times during years in 1979-2006 [38]

.

resources (like solar energy) which could cover all the power demand in the Earth.

2. In contrast to conventional wind turbines, the AWE devices are able to reach higher altitudes where the wind is not only more stable but stronger.

3. As it has been shown, the power generated increases by the cube of the wind speed. Therefore increasing a little bit the altitude may produce a lot more power.

4. As it was illustrated with the example of the A380 wing, AWE devices will be significantly less massive than traditional wind turbines, providing a higher power to mass ratio. And this means huge saves in material and therefore in costs.

5. While wind turbines are fixed to the ground, AWE systems may be thought to be carried to places where more power delivery is needed depending on the situation. In fact, there are some ideas under development taking into account the mobility of AWE systems, as it is mentioned in Chapter 2.

6. Another important advantage may be the low acoustic and visual impacts since airborne devices are thought to fly at altitudes typically greater than 200 m. Therefore they are less visible and audible from the earth than conventional wind turbines for example.

1.2.5 Limitations of Airborne Wind Energy

As it has been shown, AWE presents many advantages as a renewable energy resource. However it also has some potential limitations that have to be taken into account:

1. Wind is always present but it is not always constant in time. This may cause a problem when continuous power delivery is required. The same could happen due to inclement weather, since at these conditions AWE systems may be inoperative. In order to solve this potential problem, two main solutions could mitigate the impact on the lack of power production:

   a) The use of batteries whenever the production during productive time is sufficiently large to store energy.

   b) The installation of ground based transmission lines between AWE farms in order to transmit electrical power from productive farms to non-productive ones when needed [41].

2. Geophysical limits to global wind power. If AWE was used as one of the main energy resources to supply the world's power demand, the presence of AWE devices in the atmosphere would be on a broad scale. This would add a lot of drag forces that would remove momentum from the atmosphere in a global climate model. As the number of flying devices increases over large geographic regions, power extraction first increases linearly until it converges to a saturation potential (infinite drag, motionless atmosphere). This would be the geophysical limit to global wind power.

   According to some researches [54, 58], it seems that in a close future this limit would not be a problem even if the AWE would satisfy all the world's energy demand. The evolution of wind energy would be determined by economic, political or technical constraints rather than global geophysical limits [58]. Even though, more realistic studies might be done to assure this.

3. Finally, like any flying device, AWE systems present some risks related to collisions in the airspace. But furthermore these systems have tethered devices, which implies some added risks. Principal potential hazards of AWE systems related to the presence in the airspace are [63]:

   a) Uncontrolled crash attached to the tether(s)

   b) Uncontrolled crash detached from the tether(s)

   c) Uncontrolled fly away (with tether(s) partly still attached)

   d) Collision of the wing with General Aviation

   e) Collisions of General Aviation with the tether(s)

f) High speed rotor failure

g) High voltage exposure

1.3 Problem statement. Objectives of the project

There is a line of research at Universidad Carlos III de Madrid which is devoted to the development of AWE using power kites. It is apparently the only one active on this field in Spain. The project, funded by the Ministry of Economy and Competitiveness of Spain, is called "Simulation and Flight Testing of Power Kites applied to Wind Power Generation". The research group, formed by professors, students and associated researchers, counts on two kite-surf leading edge-inflatable kites of different sizes: 10 m^2 and 13 m^2 respectively (Figure 1.6). These kites are provided with several on board instrumentation (inertial navigation unit) and they are joined to a control bar (Figure 1.7) by means of four tethers: two tethers attached to the leading edge and two control tethers attached to the trailing edge. There is still no ground station to generate useful power since the project is in the first stages of its development.

FIGURE 1.6. Example of power kite used at UC3M

FIGURE 1.7. Kite control bar used at UC3M

For the time being several theoretical and experimental advances have been done during the last years since the research started. A simulator of a two-line kite has been developed [65] and another one of a four-line kite is in progress. The midterm goal of the research is to combine experimental results and simulations to characterize the aerodynamic coefficients associated to the kites. Thus some experimental tests have been carried out. In [67] the preliminary results of some tests are shown. However, they can be further improved by making progress with the hardware of the AWE system. This is the main objective of this bachelor thesis.

The purpose of this thesis is on the one hand to characterize both kites in order to get some geometrical and inertia characteristics. This data will be used in the future as inputs for the Matlab simulator. On the other hand, to design, construct and implement a meteorological station provided of a set of sensors that allows to know the velocity of the wind (direction and magnitude). This improvement will be useful to calculate in a close future the aerodynamic

velocity of the kite (velocity of the kite with respect to the mass of air), which until now has not been properly estimated in the experiments with these kites. Equation 1.8 shows the definition of the aerodynamic velocity, which is the difference between the ground or absolute velocity (velocity of the kite with respect to the ground) and the wind velocity.

$$\vec{V}_{aerodynamic} = \vec{V}_{ground} - \vec{V}_{wind} \tag{1.8}$$

Summary of the objectives of this thesis:

1. Characterize two kitesurf kites using a CAD software.
2. Design and implement a weather station aimed to provide the wind velocity vector close to the ground.
3. Estimate the wind velocity at the height of the kites.
4. Calibrate and test the weather station.

1.4 Methodology

The methodology to design the meteorological station will follow the philosophy of a Systems Engineering process. According to [61], a system is " a construct or collection of different elements that together produce results not obtainable by the elements alone", thus the meteorological station can be considered a system. The value of the whole lies in the interconnection of all its individual parts.

Systems Engineering is an engineering discipline whose purpose is to define a process to develop a system successfully. This process is usually composed of the following stages, which occur in parallel as it is shown in figure 1.8:

- State the problem : define the needs and requirements.
- Investigate alternatives : think about possible solutions to the needs in terms of cost, efficiency, risk...
- Model the system : model the different alternatives.
- Integrate the system : integrate all the elements of the system in order to interact with one another to work as a whole.
- Launch the system : run the system and produce outputs.

- Assess performances : analyse the outputs.
- Re-evaluate : this stage is done after each of the stages before mentioned.

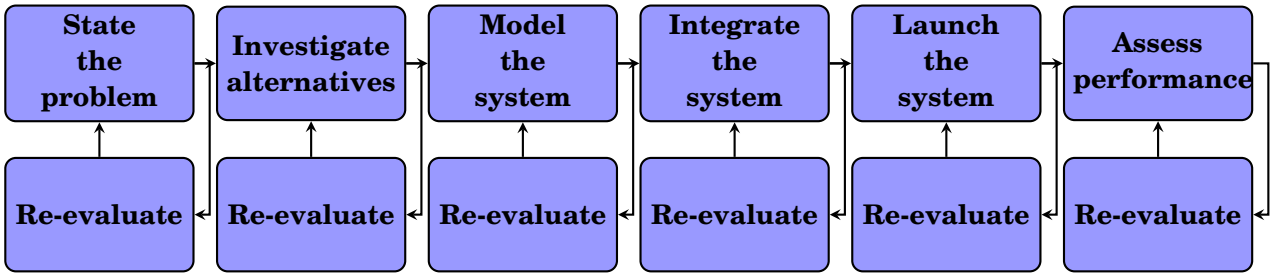

FIGURE 1.8. SIMILAR process of Systems Engineering [61]

.

1.5 Time planning

One of the keys to success in a project is to develop a detailed time planning prior to start working on it, in order to organize all its phases and assure it is completely finished before the deadline. The time planning for this project has been graphically exposed in a Gantt diagram that can be observed in Figure 1.5.

1.6 Budget

This section is devoted to describe the costs associated to the project. They are divided as follows:

1.6.1 Personal expenses

According to [32] the basic salary of a technical engineer in Spain is at least 10.25 €/hour. Assuming a working time of approximately 400 hours, the total personal expenses come to 4100 €.

1.6.2 Software cost

For the development of the project the following programs have been used:

- Solid Edge V9 Student version → Free licence
- Matlab 2016 → Free licence for students at UC3M
- QGC-Qgroundcontrol → Free, open source software available for Windows

Therefore there are no software costs associated to this project.

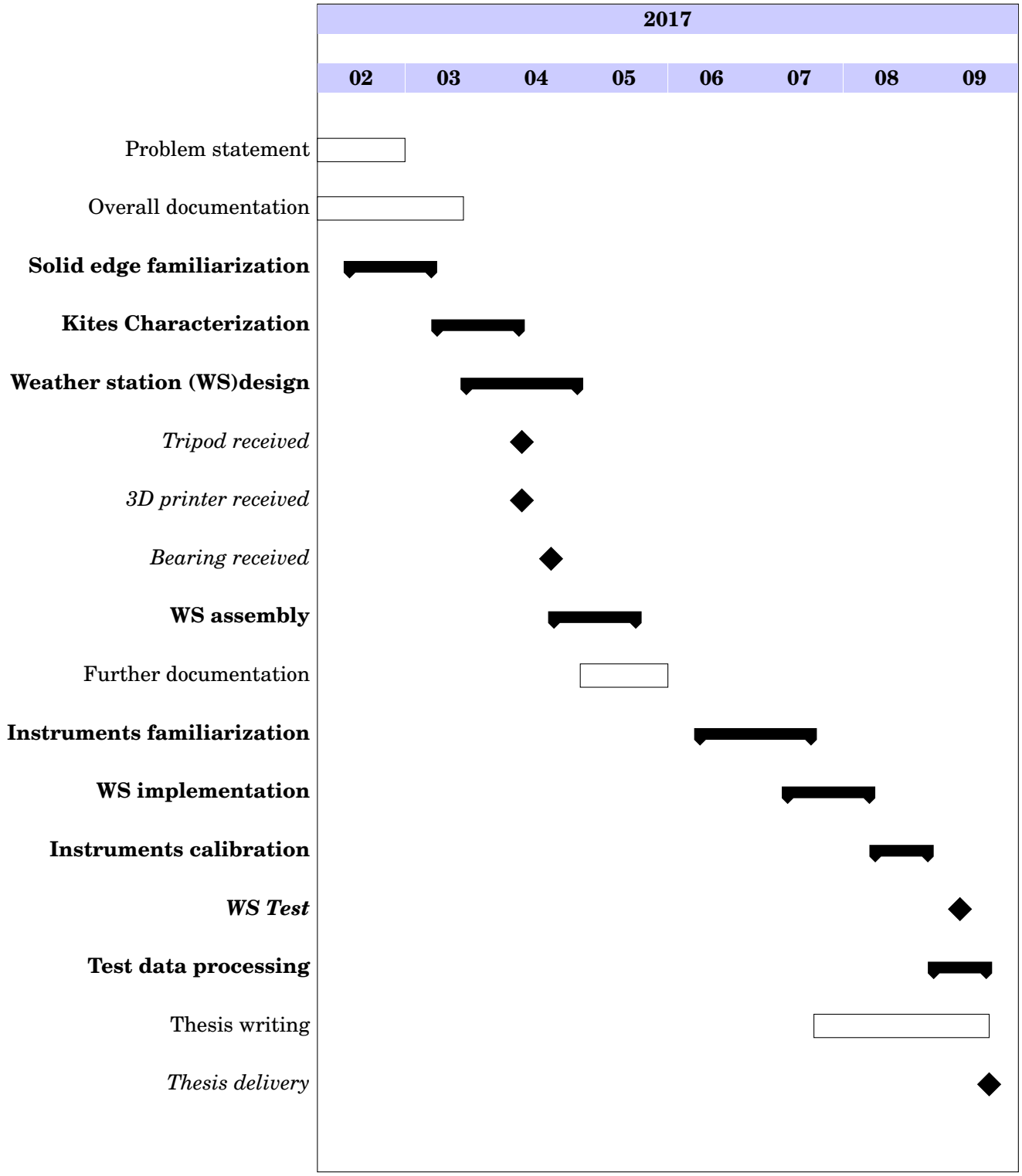

Figure 1.9: Gantt diagram of the project

1.6.3 Hardware cost

Table 1.1 shows the cost of the components used in the project. The total cost of the hardward amounts to 3970€, and the total cost of the project can be estimated as 8070 €.

Component	Unitary price [€]	Units	Total cost [€]
Tripod	225	1	225
Bearing	25	1	25
PC	800	1	800
3D printer + PLA material	2500	1	2500
3DR Pixhawk + 3DR uBlox GPS with Compass Kit	339	1	339
Pixhawk Airspeed Sensor Kit	79	1	79
Aluminum bar	2	1	2

TABLE 1.1. Hardware costs of the project

CHAPTER 2

STATE OF THE ART

The present chapter is aimed to provide information of the current state of the Airborne Wind Energy environment. For this purpose, first of all an analysis of the different types of AWE systems will be done pointing out the most important industry highlights. Moreover, the AWE field will be discussed with regard to the socio economic and legal frameworks.

2.1 AWE Industry highlights

The Airborne Wind Energy generation can be divided in two main groups: ground-gen and fly-gen, as it was mentioned in Chapter 1.

2.1.1 Ground-gen AWE systems

The basis of GG-AWE systems is to take advantage of the aerodynamic forces generated at the aircraft, mainly lift when it is combined with crosswind motion. This is the reason why Ground-gen mode is also known as *lift mode*. These aerodynamic forces produce a tension on some ropes or tethers which are connected to a ground station that can be either fixed or moving. The type of ground station and the type of aircraft used in the GG-AWE system will determine its efficiency and cost, among other aspects. In the following sections the different combinations of aircraft and ground station that are being currently developed will be exposed.

2.1.1.1 Types of aircraft in GG-AWES

The selection of the aircraft for a GG-AWE system is a paramount aspect of its design. The designer can choose a flexible aircraft, a rigid aircraft or a combination of the two depending on the requirements of the design. Basically, the higher the rigidity of the aircraft, the higher the

efficiency but also the weight penalty and the damage caused in case of failure. Therefore the design is a trade-off between several aspects summarized in table 2.1.1.1.

Rigidity	**Efficiency**	**Speed**	**Weight**	**Potential danger**	**Cost**
High	✓	✓	X	X	X
Low	X	X	✓	✓	✓

TABLE 2.1. Trade-off aspects in the design of an aircraft for a GG-AWE system. Note that the check mark implies an advantage whereas the cross mark means the opposite.

The main prototypes of aircraft under development in the field of GG-AWE systems taking into account the considerations exposed are the following:

1. Leading edge inflatable (LEI) kite
   This kind of single layer kite keeps its shape due to the lift generated on it. Its main advantage is its light weight and its easy of handling. Moreover, due to its lightness it can be operated without causing major damage in case of failure and due to its flexible nature, no structural forces compromise the integrity of the wing. There are two basic types of LEI kites: *Supported Leading Edge (SLE)* kites (Figure 2.1a) and *C-kites* (Figure 2.1b). The main difference between both types is the way in which bridles are located on the kite. SLE kites have a central bridle that flattens this part of the kite, increasing the aerodynamic efficiency.

2. Foil kite
   These kind of aircraft consist on a double layer kite made of canopy cells that are open at the leading edge. When the kite is flying, the air inflates these cells. This is the reason why this kind of kites are called ram-air kites. They have the same advantages as the LEI kites due to its flexibility and lightness. However foil kites provide a better aerodynamic efficiency. An example of this kite is shown in Figure 2.1c.

3. Delta kite
   This kind of wing is simply a single layer kite with delta shape reinforced with a rigid frame. This extra rigidity causes the appearance of some undesirable bending moments on the structure, thus making necessary the use of spars that increase the weight of the wing. Despite of this fact, delta wings provide a higher efficiency than LEI kites or foil kites.

4. Glider
   A glider is a rigid aircraft and therefore it is subjected to the appearance of bending moments, as it is the case of the delta kites. Moreover, their cost is higher. However they have a better performance. An example of a glider used in the AWE field is shown in Figure 2.1d.

5. Swept rigid wing
   Again, since this type of wing is rigid it presents similar advantages and disadvantages as the glider. However, wing sweep has the effect of improving performance since it delays the shock waves caused by compressibility effects that may appear during flight. Figure 2.1e shows an example of swept rigid wing. Note how the bridles are connected in order to control the stability of the aircraft.

6. Semi rigid wing
   This kind of wing tries to combine the advantages of rigid wings (high efficiency) and the ones provided by flexible wings (lightness, reduced cost and potential damages). As it can be observed in Figure 2.1f, this prototype consists of a set of thin rigid panels combined to have the shape of a flexible kite.

7. Tensairity
   With the same purpose of the semi rigid wings, the *tensairity* concept is being tested. The basis of this idea is to combine an airbeam with conventional cables and struts to improve the load bearing capacity of inflatable structures [43].

8. Aerostat
   Different from any other prototype above presented, there is a type of AWE system that uses an aerostat like the one shown in Figure 2.9. It is a cylinder filled with helium, thus lighter than air, which is its main advantage. However, the velocity reached by this craft is very low so it cannot provide high power deliveries.

2.1.1.2 Types of aircraft control in GG-AWES

Once the aircraft is designed, the next step is to decide how it is going to be controlled. There are several options currently under development which are summarized in Figure 2.2. The stability and trajectory of the aircraft can be controlled using several types of control systems [44] [59]. The most common are:

- Two power lines (Fig.2.2c): this is the most simple control system that can be used to drive a kite. The length of the lines can be modified in order to change the direction of the aircraft. However, the angle of attack cannot be controlled.

- Three power lines (Fig.2.2d): adding a third control line at the leading edge of the aircraft the angle of attack can be modified thus allowing to change lift. The lateral lines act in this case as control lines to direct the kite.

- Single line tether with control pod (Fig.2.2b): the two previous systems can be improved by merging the lines into a control pod, which is a flying control box provided of one or more

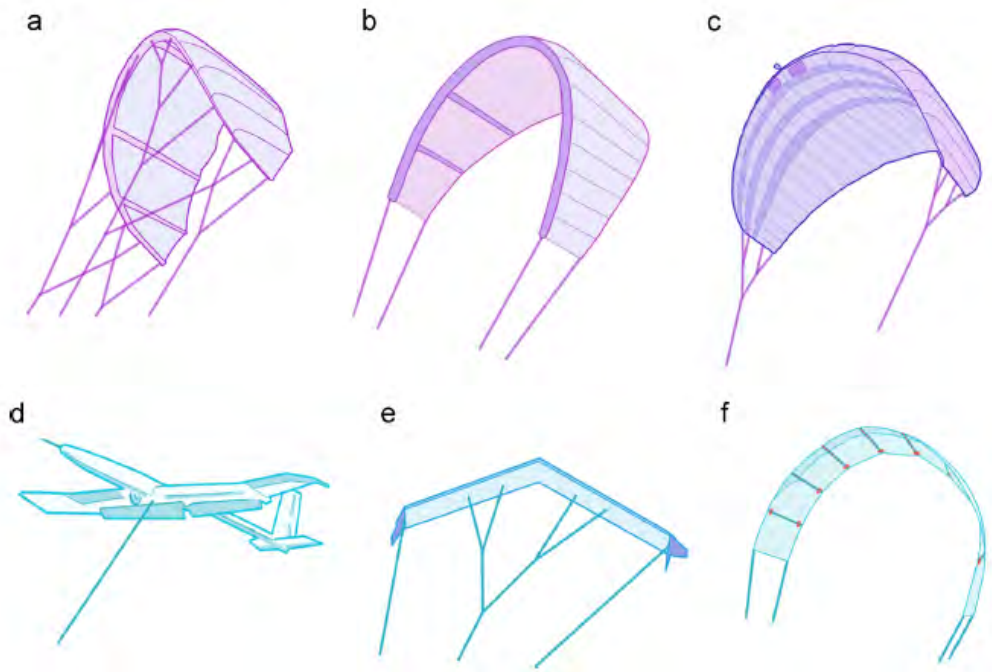

FIGURE 2.1. Types of aircraft used in Ground-gen AWE systems. Figure from [44].

actuators acting as a steering unit. The micro-winches inside the control pod allow to steer the kite by pulling or pushing the lines and also to modify the angle of attack in the case of a three-line control system.

- On-board actuators (Fig.2.2a): rigid and semi-rigid aircraft can be provided of on-board actuators to control aerodynamic surfaces such as ailerons for flight control.

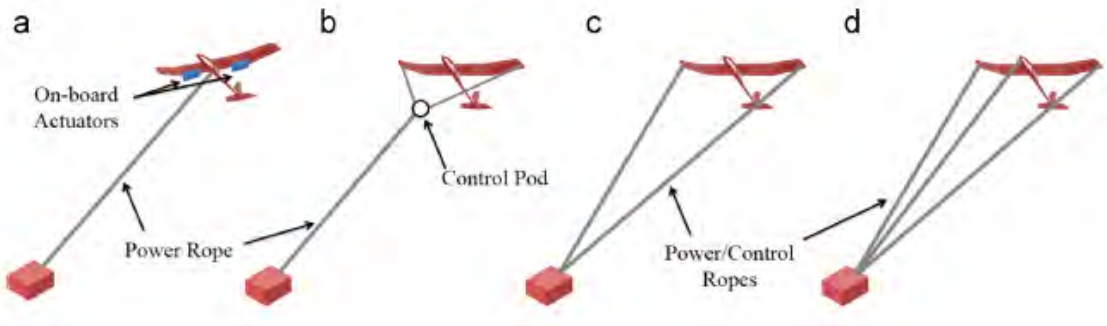

FIGURE 2.2. Types of aircraft control used in Ground-gen AWE systems. Figure from [44].

2.1.1.3 Fixed ground station GG-AWE systems

The most common type of Ground-gen AWE system has its ground station fixed. The power generation takes place in a two-phase process shown in Figure 2.3. First of all the tether is subjected to tension due to the aerodynamic forces acting on the aircraft. This tension produces the unroll of the tether from a drum which drives an electric generator. This first phase in which electric power is produced is called *reel-out phase*. The second phase consists on retracting the tether so that it can be unrolled again. The recovery phase is called *reel-in phase*, and evidently consumes some energy. However, the amount of energy used in the retraction phase is much lower than that produced in the generation phase . Due to the continuous reel-in and out of the tether, this kind of AWE generation is usually called *pumping mode* or even *yo-yo mode*, and fixed ground station GG-AWE systems are known as *Pumping Kite Generators*. During the *reel-in* phase, the aircraft can be either static or moving describing a determined path. In the majority of the cases, the pumping mode is combined with crosswind power in order to improve the efficiency of the system. In these cases the aircraft takes advantage of the crosswind and describes eight-shaped paths as it is shown in Figure 2.3. In this way a strong apparent wind is induced increasing the tension on the tether. On the other hand, there are some prototypes in which the pumping generation does not take advantage of crosswind power but from the Magnus effect. A brief description of some prototypes currently under development using GG-AWE systems will be exposed in order to establish a comparison between them. The entities in charge of these prototypes are the following:

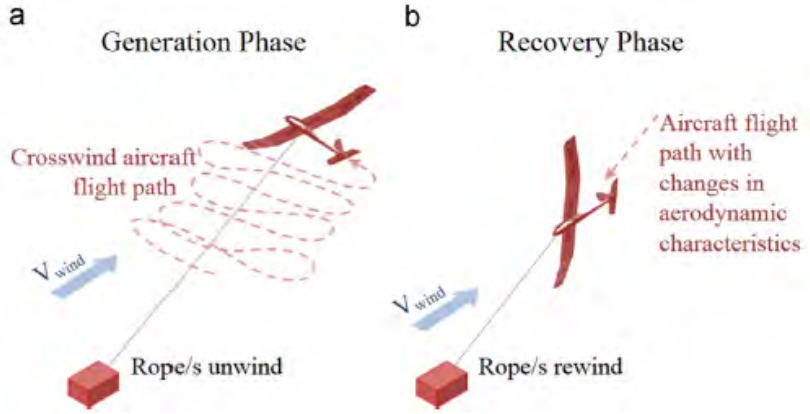

FIGURE 2.3. Different phases to produce electric power in pumping GG-AWE systems. Generation phase or *reel-out* (a) and recovery phase or *reel-in* (b). Figure from [44].

- **Ampyx Power**

  The Dutch company Ampyx Power [5] is the first one in the field of AWE which has implemented and proved a fully functional autonomous glider able to generate electric power taking advantage of crosswind. This is the AP-2 model (Fig. 2.4), capable of producing

up to 10 kW of average power with peaks of 15kW [64]. It is an aircraft provided of on-board controlled surfaces (rudder, elevator and flaperons) which can land and take off from a ground station provided by a catapult system for take off. The aircraft is joined to this station through a strong tether and has also a propulsion system to climb aid. The AP-2 model is able to generate power fully autonomously and continuously with a maximum endurance of two hours.

Currently the company is working on the development of a more ambitious prototype called AP-3, which is aimed to be functional during the course of 2018. This new model consists of a twin-fuselage aircraft made of composite material provided of several control surfaces such as ailerons, flaperons, a tail rudder and an elevator, a retractable landing gear and triple redundant avionics. It will land and take off using a rotative platform (Fig. 2.5) that aligns with wind direction in order to reduce ground speed during launch and landing. This model is aimed to provide up to 250kW.

FIGURE 2.4. Ampyx Power AP-2 model already implemented. Figure from [5] .

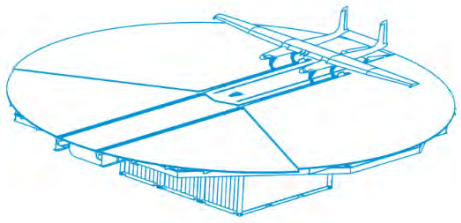

FIGURE 2.5. Ampyx Power AP-3 prototype currently under development. Figure from [5].

- **TwingTec**

This Swiss company [25] is developing a fully autonomous glider with embedded rotors called TT100, which is aimed to generate up to 100kW. The aircraft lands and take off using these rotors perpendicular to the wing surface, and flies describing 8-shape patterns reeling in and out two lines joined to a compact ground station which can be easily installed and transport. Figure 2.6 shows the TT100 model.

- **EnerKite**

The company EnerKite [9], founded in Germany, is carrying out several lines of investigation in the field of AWE. First of all it has developed a system that produces up to 30kW continuously (the EK30 model) using a foil kite controlled from the ground. On the other

hand they are also working on the development of a delta aircraft with three control lines which is expected to produce 200kW (EK200 prototype, Fig. 2.7).

- **SkySails Power**

  SkySails Power [24] is a division of the German company SkySails. This company was born in 2001 to develop propulsion systems for cargo vessels based on the use of kites. However a few years ago it started to apply these systems in the field of AWE generation. The system that drives the vessels consists of a foil kite that takes advantage of the crosswind while it is controlled by a pod (Fig. 2.8). The same configuration is being developed in the AWE generation. SkySails has also developed and patented a launch and recovery system composed by a telescopic mast that is able to grab and release the leading edge of the kite [50]. Expected production of power with these AWE systems is up to 3.5MW.

FIGURE 2.6. TwingTec TT100 model. Figure from [25].

FIGURE 2.7. EnerKite EK200 currently under development. Figure from [9].

- **TU Delft**

  Delft University of Technology is one of the most committed entities to the AWE research. A couple of years ago this university organized a conference (AWEC 2015, [3]) in which the most important progresses done in the AWE generation were exposed. With regard its advance in the field, TU Delft has developed a single tether LEI kite capable of producing 20kW. As SkySails, it is also controlled by a control pod. An automatic launch and retrieval system is also under development at this university.

- **Omnidea**

FIGURE 2.8. SkySails kite propulsion system. Detail of the control pod. Figure from [55] .

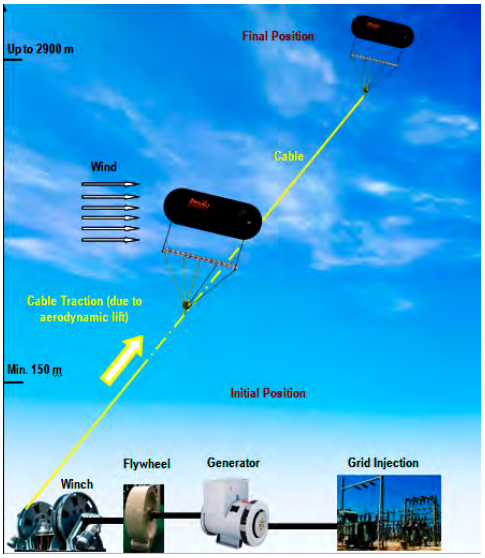

FIGURE 2.9. Omnidea aerostat exploiting the Magnus effect. Figure from [18].

The Portuguese contribution to the AWE comes by the hand of the company Omnidea, which has bet on aerostats to generate power taking advantage of the so called Magnus effect (Fig. 2.9).

2.1.1.4 Moving ground station GG-AWE systems

Besides fixed ground station GG-AWES, there are some concepts in which this station can move on the ground allowing the system to generate power continuously since the recovery phase is cut out. There are two different types of moving ground station GG-AWE system (Fig. 2.10):

1. *Vertical axis generator*

   In this concept several power kites are joined to small ground stations which are in turn fixed to a common moving ground station. This moving ground station is the rotor of an electric generator. Therefore the electric power is produced due to the torque generated at the rotor by the kites. An example of this system is being studied by the company KiteGen, which is working on the development of a carousel of kites as the one shown in Figure 2.11. According to its studies this type of GG-AWE system could produce up to 1GW of continuous power in the future using a carousel of 1600m of diameter [12]

2. *Rail generator*

   In this case the power kites move ground stations integrated in rails either in a closed loop or in an open loop. The major contribution to this type of GG-AWE system is being made by the German company NTS [17], which is working on the design and implementation of

a 400 linear metre closed track (Fig. 2.12) in which a railed car is moved by a 20 m^2 kite. According to the studies of the company, a kite of 10 m^2 is able to produce 10kW of power. They are currently trying to scale up the prototype in order to improve the capacity of the system.

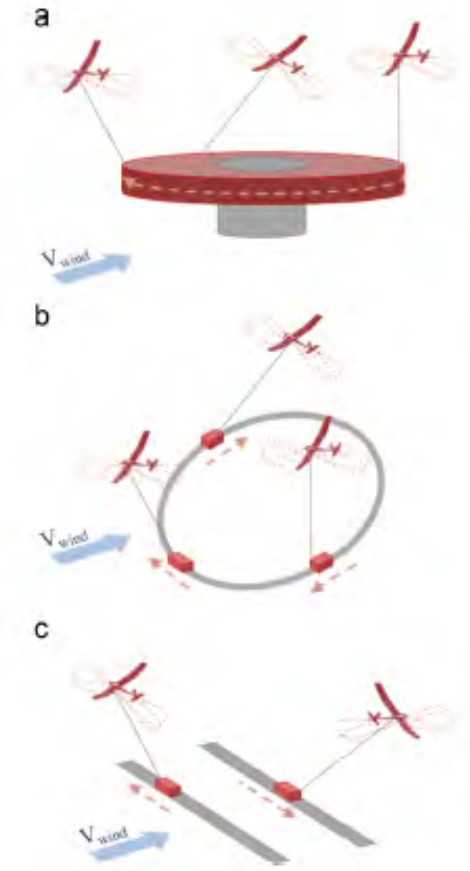

FIGURE 2.10. Types of moving ground station GG-AWE systems. a) Vertical axis generator, b) Rail closed loop generator and c) Rail open loop generator. Figure from [44].

FIGURE 2.11. KiteGen carousel. Figure from [12].

FIGURE 2.12. NTS closed loop GG-AWE Figure from [30].

2.1.2 Fly-gen AWE systems

In Fly-gen AWE (FG-AWE) systems the electric power is generated by on board turbines and it is transmitted to the ground station by means of special tethers that integrate electric wires. This kind of AWE generation is also called *drag mode* generation due to the addition of drag produced by the turbine on the aircraft. The wind turbines can generate power taking advantage of the crosswind or the absolute wind:

- Crosswind: these systems use the flying principle of the wing lift, the same used by the majority of GG-AWE systems. The most important contribution in this field of AWE systems comes by the hand of the American company Makani [15]. This company has developed a tethered aircraft provided by four Airborne Wind Turbines (AWT). During the landing phase, which takes place vertically (Fig. 2.13), the turbines act as propellers providing the necessary thrust. Then, during the flying phase the rotors act as generators while the aircraft is moving describing a circular path. Makani has already tested a 20kW prototype and has successfully generated electricity with the 600kW model (M600) provided by eight brushless CD motors [57].
- Absolute wind: in this case the systems are based in the buoyancy flying principle. Altaeros Energies [4], entity led by MIT and Harvard alumni, has already implemented a Lighter Than Air (LTA) AWE system consisting of a ring shaped aerostat filled with helium. Aerostatic lift, or buoyancy, arises from enclosing a volume V of this gas, and is proportional to the difference in the density of this gas and the surrounding air, according to equation 2.1 [70]. The conversion between the kinetic energy of the wind into electric energy is done by a Buoyant Airborne Turbine (BAT) provided by a diffuser duct which helps to accelerate the airflow.

$$F_b = V(\rho_{air} - \rho_g) \tag{2.1}$$

FIGURE 2.13. Makani Power FF-AWE prototype. Figure from [56].

FIGURE 2.14. Altaeros LTA AWE system. Figure from [52].

2.2 Current socio-economic environment

As it occurs in the case of any renewable energy type, the AWE field has to overcome several barriers in order to be able to compete with the leaders in the energy field: nuclear and fossil fuels.

And this is a hard task due to some principal reasons: these last sources provide the easiest and cheapest way of obtaining energy nowadays and they are supported by some important entities due to political reasons. On the other hand, renewable energies need a high initial investment at a high risk and this is a disadvantage that plays against its development. Moreover there exists a particular barrier added to the starting renewable energies nowadays: the vision and image of the previous generation of renewable energies (solar, wind turbines, etc), which have not turned out to work as well as expected, so investors are afraid of investing in something that may not work [48]

To better understand the socio-economic environment of the AWE field, a typical technology life cycle of a renewable energy that can be applied to the AWE is shown in figure 2.15. The AWE field is currently in different steps of this cycle, since there are several lines of development in the world. The most of them can be located in the research step, as it is the case of the UC3M. These researches have to rely on public subsidies and are carried out at universities. After that, the researchers have to be able of demonstrating that their technology actually works. That is the step in which some private investors can start to be attracted by the project. Some AWE companies previously mentioned in this chapter are currently in this step of the cycle and are financed by some so-called venture investors that provide a huge amount of capital under high risk in order to develop the project initially. An example was Makani, financed by Google, which has even surpassed this phase and has tested the world's first commercial scale AWE system [57] being able to produce electricity with it. However the most of the companies and institutions devoted to the AWE development field have not gone beyond the pre-commercial phase. Therefore in order to make its way in the industry, the AWE field has to be more attractive to investors developing their technology and reducing risk with regard to the future.

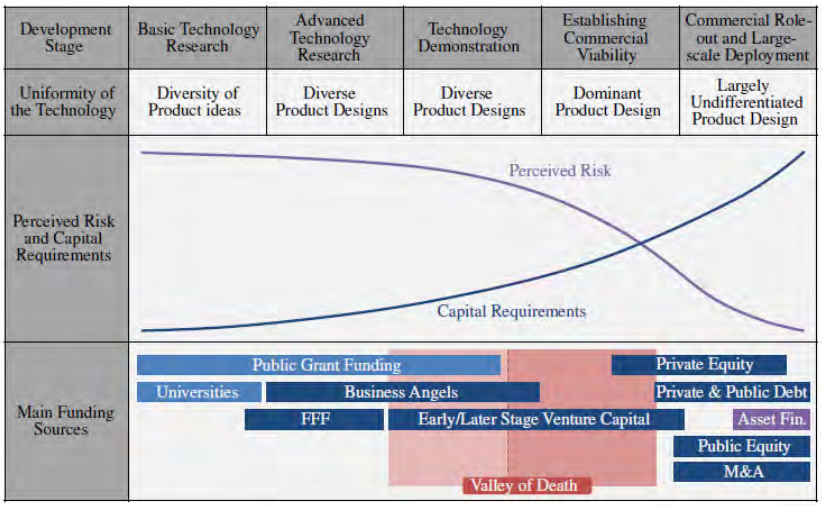

FIGURE 2.15. Technology life cycle for a renewable energy technology. Figure from [72].

2.3 Legal framework

In order to discuss about the legislative framework it is needed to take into consideration that the AWE generation is a new field which is starting to be developed. Therefore the aviation authorities have not yet been able to establish a set of regulations for this kind of systems.

On the other hand, it is important to define what an AWE system is. An AWE system is an airborne device capable of generating usable power [36]. Analysing this definition some might be led to believe that AWE systems could be considered RPA (Remotely Piloted Aircraft). This is a controversial issue and Airworthiness Authorities have different points of view regarding it. The FAA in US does not consider AWE systems as RPAS. However, EASA in the EU considers that fast heavy flying AWE systems can be treated as RPAS and can fly even higher than these systems (above 500 ft) [31] [63].

AWE devices are thought to work in class G airspace (below 14,500 feet (4,400 m))[31], which is uncontrolled so a risk of collision with General Aviation may occur. Moreover, it is important to take into account that they are tethered devices and this fact implies that a set of particular risks are added (see section 1.2.5, point 3).

Failure due to these risks may have serious consequences so this kind of systems needs a specific regulation to be certified and integrated in the airspace in a safely way. According to [63], and due to the variety of AWE systems that are currently under development, the future regulation and standardization process should be a compromise between the owner and the authorities. In order to speed up the process, the owner should firmly establish the specific risks of the AWE system to be certified. Then, the proper regulation would be carefully defined based on already implemented legislation for similar vehicles, such as RPA. Possible applicable European standards are shown in figure 2.16.

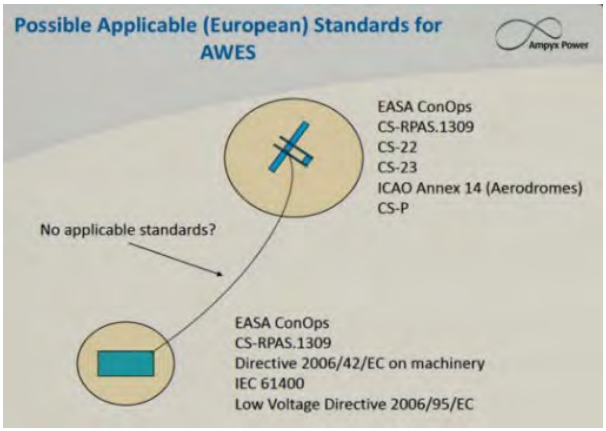

FIGURE 2.16. Possible applicable European standards for AWE. Figure from [63].

CHAPTER 3

CHARACTERIZATION OF THE KITES

As it was mentioned in the introduction of this thesis, the UC3M is currently working on the development of a kite simulator. This simulator needs to be as realistic as possible in order to provide accurate results, thus it has to use real inertia and geometrical data of the kites. One of the purposes of this project is to provide with this data in order to be able to make progress with the simulations in the close future.

This chapter is devoted to show the method to characterize both LE-inflatable kites: the small one (10 m^2) and the big one (13 m^2). It was done developing two CAD models in order to estimate their centres of mass and inertia tensors among other data. The software selected to design the models has been Solid Edge, since it offers an open-source version for students.

3.1 Methodology

In order to design the 3D models with the CAD software, the first step was to take measurements of the dimensions of the real kites. Using this data, the models were developed to meet the specified dimensions. On the other hand, the weights of the deflated kites were obtained with the aid of a simple scale. After that, the density of the material used in the software was adapted to meet the weight requirements. Table 3.1 shows the real mass of each deflated kite and the density assigned to the material used in the software for each model.

Kite	Mass of deflated kite [kg]	Density 3D model [kg/m^3]
Small	3.400	216.200
Big	3.400	183.150

Table 3.1: Properties of each kite

3.2 Frames of reference

The CAD software uses two different frames of reference. The first one is defined as 'RF1'. It is centred at point O, located on the ground at the bottom of the kite, just in the intersection between the plane of symmetry of the kite and the trailing edge plane. The x axis is pointing in the span-wise direction, the y axis in the direction of the chord and the z axis in the vertical one.

On the other hand, the software uses a second reference frame whose axes are the principal axes of inertia of the body about its centre of mass G, which is the centre of this frame. In this case the axes are numbered from one to three, being β the angle of rotation between this frame and RF1, as shown in Figure 3.1. Both frames of reference can be seen in Figures 3.1 and 3.2.

3.3 CAD models

Both 3D models were designed combining a set of surfaces: swept surfaces to simulate the inflatable elements (leading edge and ribs) and a bounded surface for the body. A thickness of 1 mm was given to each model in order to convert it into a solid. The following sections show the models and properties of both kites.

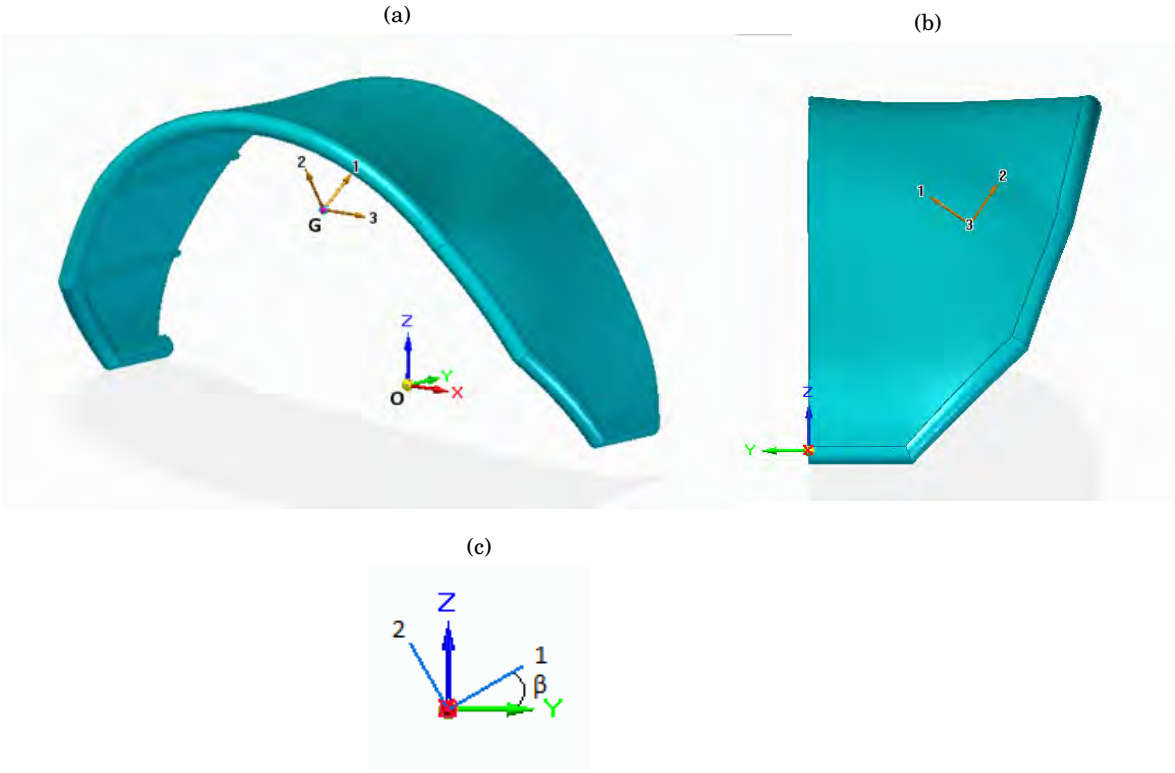

FIGURE 3.1. Position of the centre of mass in the small kite CAD model

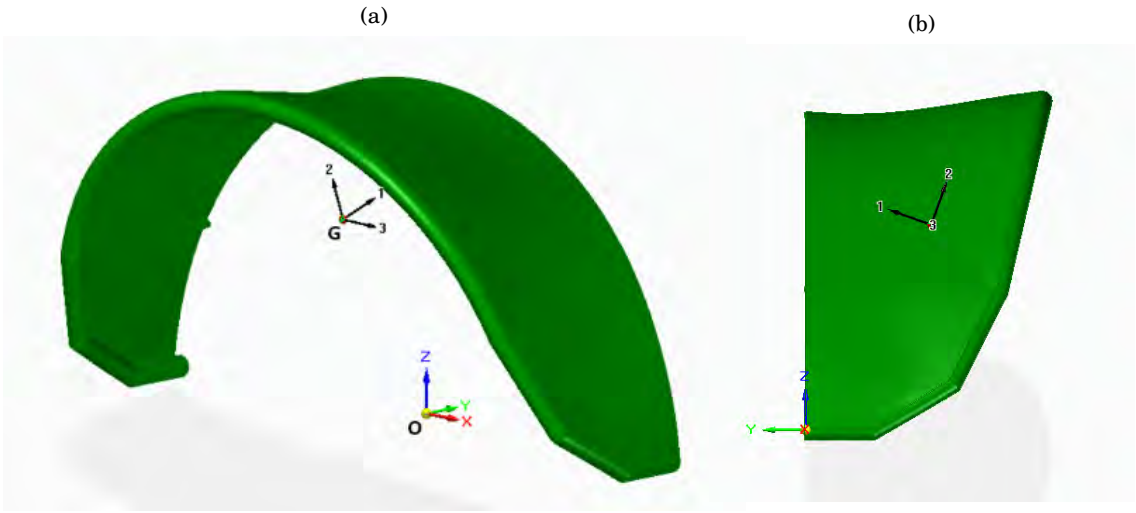

FIGURE 3.2. Position of the centre of mass in the big kite CAD model

3.3.1 Mass properties

Table 3.2 shows the location of the center of mass with respect to frame of reference RF1, as well as the angle of rotation β in each case.

Kite	$\vec{x}_G$ **(in RF1) [m]**	β **[degrees]**
Small	-0.9794 $\vec{j}$ + 1.3751 $\vec{k}$	34
Big	-0.9797 $\vec{j}$ + 1.5962 $\vec{k}$	21.5

Table 3.2: Center of mass and angle of rotation β for both models

It is also interesting to know how the mass is distributed in the kites. The software provides the inertia tensor of each kite projected in its principal axes (PA) about its center of mass (G). These inertia tensors are given by:

$$\bar{\bar{I}}^{small}_{PA,G} = \begin{bmatrix} I_1 & 0 & 0 \\ 0 & I_2 & 0 \\ 0 & 0 & I_3 \end{bmatrix} = \begin{bmatrix} 8.900 & 0 & 0 \\ 0 & 8.179 & 0 \\ 0 & 0 & 2.434 \end{bmatrix} kgm^2 \tag{3.1}$$

$$\bar{\bar{I}}^{big}_{PA,G} = \begin{bmatrix} 12.501 & 0 & 0 \\ 0 & 11.241 & 0 \\ 0 & 0 & 3.180 \end{bmatrix} kgm^2 \tag{3.2}$$

The principal axes of inertia about G are body axes but they do not correspond with the ones used in Flight Mechanics. The Matlab simulator uses a body axes reference frame such that the

x coordinate is in the direction of the chord of the kite, the y in the span-wise direction and the z coordinate pointing downwards. Therefore a rotation has to be made to transform the inertia tensors projected in principal axes into tensors projected in the interesting body axes. In figure 3.3 the relation between these two frames can be seen.

(a)

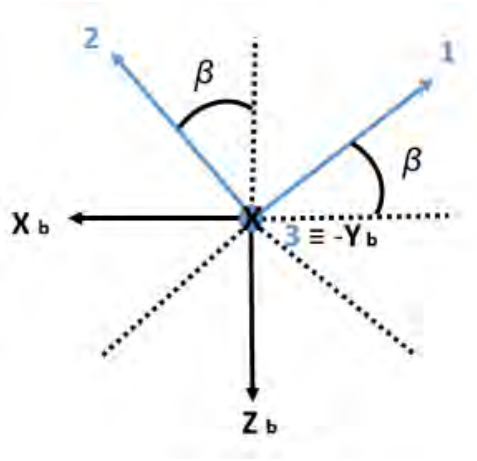

FIGURE 3.3. Relation between principal axes 123 and body axes $x_b y_b z_b$ used in Flight Mechanics

Since calculations are made with tensors, equation 3.3 has to be used, where R represents the rotation matrix needed to rotate the reference frame in which the inertia tensor is projected, and R^T is its transpose.

$$\bar{\bar{I}}' = R\bar{\bar{I}}R^T \tag{3.3}$$

The previous equation can be expressed in this particular case as:

$$\bar{\bar{I}}_{B,G} = R_{B\to PA}\bar{\bar{I}}_{PA,G}R^T_{B\to PA} \tag{3.4}$$

where $\bar{\bar{I}}_{B,G}$ is the desired tensor of inertia projected in body axes (B) used in Flight Mechanics about the centre of mass G and $R_{B\to PA}$ is the transformation matrix between body axes and principal axes defined as:

$$R_{B\to PA} = \begin{bmatrix} -cos\beta & sin\beta & 0 \\ 0 & 0 & -1 \\ -sin\beta & -cos\beta & 0 \end{bmatrix} \tag{3.5}$$

Finally, inertia tensors projected in the desired body axes about the centre of mass of the small and big kites are, respectively:

$$I_{B,COM}^{small} = \begin{bmatrix} 8.675 & 0 & 0.334 \\ 0 & 2.434 & 0 \\ 0.334 & 0 & 8.405 \end{bmatrix} kgm^2 \tag{3.6}$$

$$I_{B,COM}^{big} = \begin{bmatrix} 12.332 & 0 & 0.430 \\ 0 & 3.180 & 0 \\ 0.430 & 0 & 11.410 \end{bmatrix} kgm^2 \tag{3.7}$$

It can be observed that the products of inertia P_{xy} and P_{zy} (and therefore P_{yx} and P_{yz}) are zero since the kite is symmetric with respect to the plane $x_b z_b$, which is normal to y_b axis. These will be the tensors of inertia that will be used as inputs in the simulator.

3.3.2 Additional data

It has to be mentioned that the model used in the simulation considers the kite as a semi-ellipse as the one shown in Figure 3.4. The geometry of the semi-ellipse is defined by the parameters:

- c: mean geometric chord of the real kite
- b: span of the real kite
- h: maximum height of the real kite

Therefore, in addition to the previous data, some parameters related to the geometry of the kites are needed to be used as inputs in the simulator. The mean geometric chord ($\bar{c}$), surface and span of the kites have been gathered in Table 3.3. The mean geometric chord has been computed using equation 3.8, where y is the coordinate y used in RF1 in the opposite sense, and y_{max} is the largest value of the chord in each kite, which corresponds to the chord of the largest rib (the one at the top, in the symmetry plane of the kite). The span of the kite is considered as the distance between the two extremes as shown in Figure 3.4. The surface of the kite is given by the manufacturer.

$$\bar{c} = \frac{\int_0^y c(y)dy}{y_{max}} \tag{3.8}$$

Kite	**Surface, S [m^2]**	**Span, b [m]**	**MGC, $\bar{c}$ [m]**	**Max.height, h [m]**
Small	10	4.3	1.4	2.2
Big	13	5.0	1.5	2.5

Table 3.3: Geometry of each kite

(a)

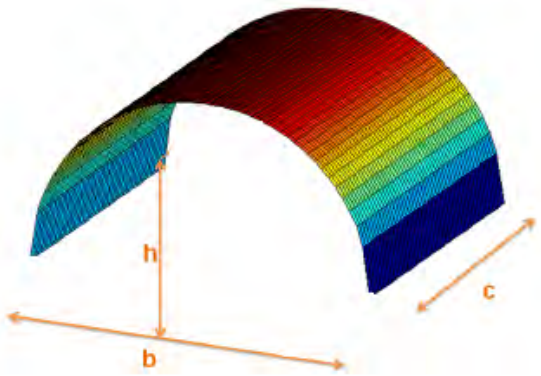

FIGURE 3.4. Semi-elliptical model of the kite used in the simulator

Finally, in order to simulate the models, some data related to the control bar and the tethers is needed. The real elements have been dimensioned. The dimensions of the control bar are gathered in Figure 3.5. Regarding the tethers, their lengths are:

- Length of LE tethers: 21.45 m
- Length of TE (control) tethers: 22.48 m

(a)

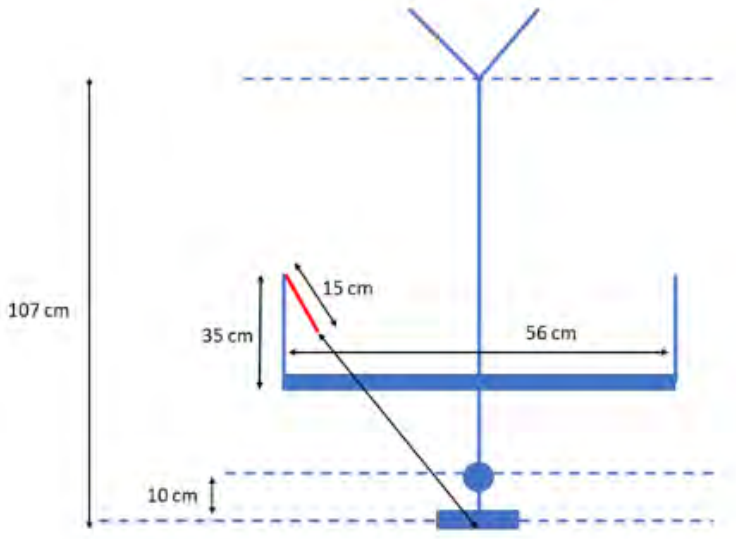

FIGURE 3.5. Control bar dimensions

The tethers are connected to the kites by means of some bridles attached to the leading and trailing edge of the kites. Their dimensions and height with respect to RF1 frame are the following ones:

Small kite:

- LE bridles: 2.40 m located at z=0.80 m
- TE (control) bridles: 0.71 m located at z=0

Big kite:

- LE bridles: 2.92 m located at z=1.17 m
- TE (control) bridles: 0.97 m located at z=0

3.3.3 Comparison between CAD models and simulator models

In order to compare the semi-elliptical model used in the simulation and the CAD models, a comparison of the centre of mass location, inertia tensors and surface of both models has been made, assuming that the parameters of the semi-ellipse are the ones exposed in Table 3.3. Regarding the centre of gravity, it will be located in the symmetry plane, half-chord at a height h_G. The inertia tensors with respect to the principal axes of the semi-elliptical models are the ones exposed in 3.9 and 3.10, for the small and big kites respectively.

Small kite

$$\bar{\bar{I}}_{PA,semi-ellipse} = \begin{bmatrix} 9.420 & 0 & 0 \\ 0 & 8.460 & 0 \\ 0 & 0 & 2.120 \end{bmatrix} kgm^2 \tag{3.9}$$

Big kite

$$\bar{\bar{I}}_{PA,semi-ellipse} = \begin{bmatrix} 12.748 & 0 & 0 \\ 0 & 11.305 & 0 \\ 0 & 0 & 2.719 \end{bmatrix} kgm^2 \tag{3.10}$$

Kite	**S [m^2]**	h_G **[m]**	ΔS **[%]**	Δh_G **[%]**	$\Delta I_{xx,PA}$ **[%]**	$\Delta I_{yy,PA}$ **[%]**	$\Delta I_{zz,PA}$ **[%]**
Small	9.57	1.4	4.4	1.4	5.8	3.4	14.8
Big	11.88	1.6	9.2	0.2	1.9	0.6	16.9

Table 3.4: Comparison between semi-elliptical models and CAD models

Table 3.4 shows the geometrical data corresponding to the semi-elliptical model and a comparison between this data and the one provided by the CAD models. It can be observed that the differences between the CAD models simulating the real kites and the semi-elliptical approximations are small. The main difference lies in the inertia tensor. It can be due to the fact that in a semi-elliptical model the mass is uniformly distributed along the whole surface, whereas the real kites and therefore the CAD models have more concentrated mass towards the leading edge. This may be the reason why the principal axes of inertia of both kites are inclined an angle β different than zero, contrary to the principal axes of the semi-elliptical models which would be parallel to the reference frame RF1.

In the near future, the data obtained from the CAD models for the centre of gravity, tensor of inertia, span and MGC will be used in the simulations.

CHAPTER 4

WEATHER STATION DESIGN

As it was stated in the introduction of this thesis, the objective of the design and implementation of a weather station is to obtain experimentally the wind velocity vector that will be used in a close future to compute the aerodynamic velocity of the kites. This chapter is devoted to the detailed description of the weather station design. Departing from the requirements of the system, the elements and instrumentation of the weather station will be described deeply .

The key components of the weather station will be an airspeed sensor connected to a Pitot tube that measures the dynamic pressure (and therefore the magnitud of the wind speed), a magnetometer to calculate the direction of the wind velocity vector and a PixHawk controller used as a data logger for the airspeed sensor and the magnetometer. These instruments will be placed in a station designed *ad hoc* based on a conventional weather vane structure. In order to optimize costs and allow flexibility in the design, 3D impression was used to create some elements. Again, Solid Edge ST9 was the software used to design these pieces. A Ultimaker 3D printer [26] was chosen and the selected material was PLA (Polylactic Acid), a thermoplastic very easy to use thanks to its low glass transition and melting temperatures [62]. Figure 4.1 shows the printer, the material and the Cura Software [7] used during the design.

4.1 Requirements of the design

The weather station required to be designed was similar to a conventional weathercock used to measure the direction of the wind. However, a typical weathervane was not enough to obtain the wind velocity, since the magnitude of the vector $\vec{V}_{wind}$ was also needed. The requirements of the design are the following ones:

FIGURE 4.1. 3D printing kit used in the project. Figure from [26]

.

- The weather station should be placed relatively far from ground in order to avoid ground interferences.
- The system should be able to rotate freely about its vertical axis offering the least friction as possible, in order to be aligned with the wind.
- It should measure wind speeds up to 15 m/s (minimum) with the minimum error as possible.
- It should measure the wind direction with the minimum error as possible.
- The system should be able to be positioned in whatever type of surface either flat or rough and still be horizontal. It means, to provide versatility when choosing the future flight test campaigns environment.
- All the elements used to obtain data from the wind should be compatible among each others.
- The sensors used in the weather station should be compatible with the ones already used on-board the kites.
- Measured data should be logged with a maximum interval of 1 millisecond.

Nowadays there is not any device already designed in the marked able to fulfill the previous requirements. Therefore an *ad hoc* design was carried out taking advantage of the versatility of 3D impression. An image of the final weather station model is shown in Figure 4.3. Its shape

reminds a conventional weathervane, however it is provided with several elements that make it different.

A typical weathercock consists of an arrow mounted on a vertical pivot. The principle of its functioning is the inequality of the yawing moment produced by its tail and its head about the vertical axis. The moment ($\vec{M}$) of a force is proportional to the force ($\vec{F}$) itself and the distance ($\vec{r}$) between the point of application of the force and the point about it is calculated (Equation 4.1).

$$\vec{M} = \vec{r} x \vec{F} \tag{4.1}$$

In the case of a weather vane the tail produces a greater moment about the vertical axis than the head, either because it has a greater area (and therefore produces a higher total force) or because the moment arm is greater, or both simultaneously. Since the tail gets pushed away from the direction the wind is coming from, the head is turned to be aligned with the wind (Figure 4.2). This is in fact the basis for the rotation of the weather station. However this rotation has to be quantified in order to know the exact orientation of the system, and also the strength of the wind has to be measured. Thus several elements have to be added to a weather vane-based system in order to reach these objectives. In the following sections the elements of the weather station will be described in depth.

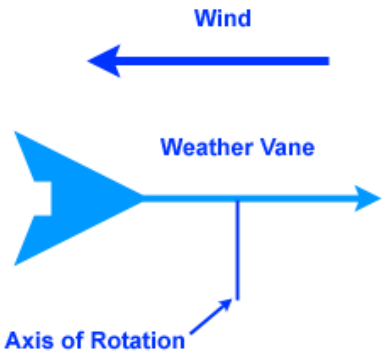

FIGURE 4.2. Weathervane fundamentals.

4.2 Elements of the model

The weather station is composed by four main elements: a head that holds the instrumentation and rotates as a conventional weather vane, a support to hold the head, a weather vane arrow that allows the head to align with the wind and finally the required instrumentation to measure the wind velocity.

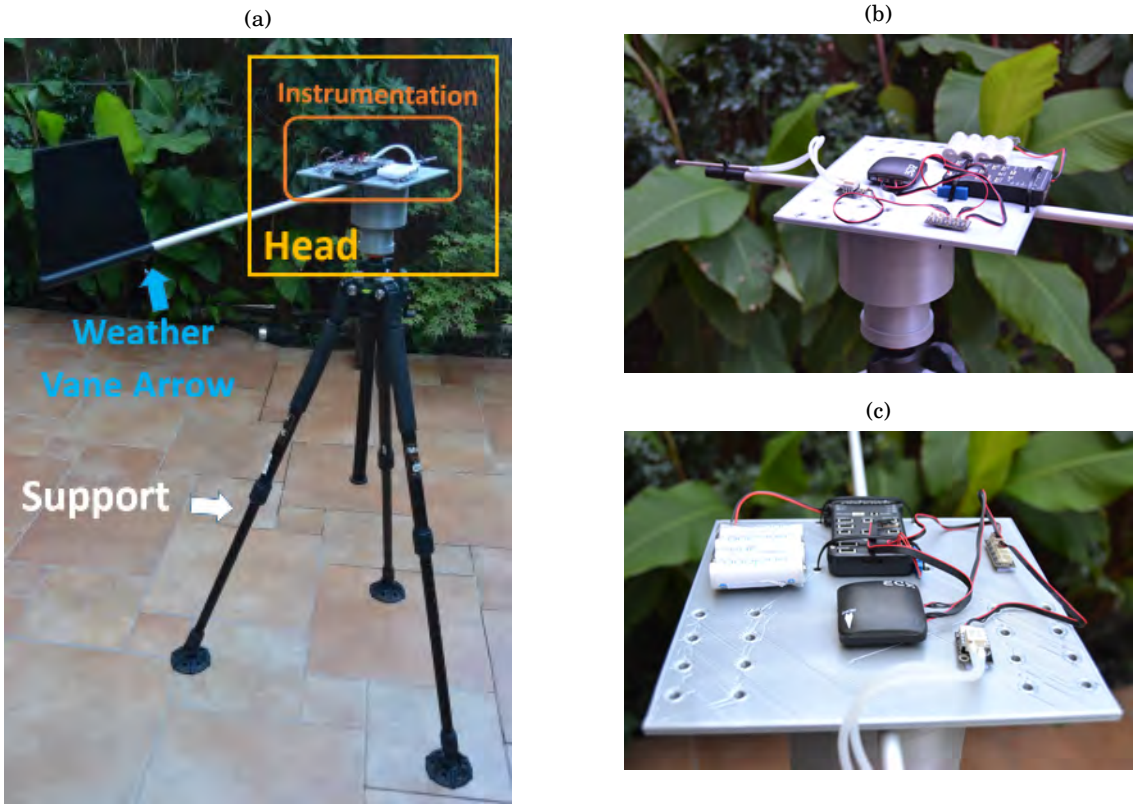

FIGURE 4.3. Final model of the weather station.

4.2.1 Support

As it has been previously mentioned, some of the requirements of the system were to be placed relatively far from ground and to be stable in any kind of surface. Taking into account these two requirements it was decided that the better solution to fit them was the use of a tripod. In this case, the tripod shown in Figure 4.4 was chosen. Spreading its legs and neck [Figure 4.5(c)] to the maximum allowed, the maximum height reached by this device is 1700 mm.

On the other hand one of the most interesting characteristic of this tripod is its robustness. Its legs end up with a grip rounded surface [Figure 4.5(d)] that can not only provide with stability to the tripod but also to grip the ground avoiding undesired movements. It is provided with a bull's eye level [Figure 4.5(b)] in order to assure that the weather vane is totally horizontal. Moreover, it is light (3.32 kg) and it can be folded to make easier its transportation during the future flight test campaigns.

It has to be mentioned that its head (where cameras are usually placed) is a small rounded base with a central screw thread and two smaller holes on each side [Figure 4.5(a)]. The central screw thread is fixed to the head so it was needed to find the way of taking it into account when designing the part that connects the tripod to the weather vane head.

FIGURE 4.4. Weather station support [27]

.

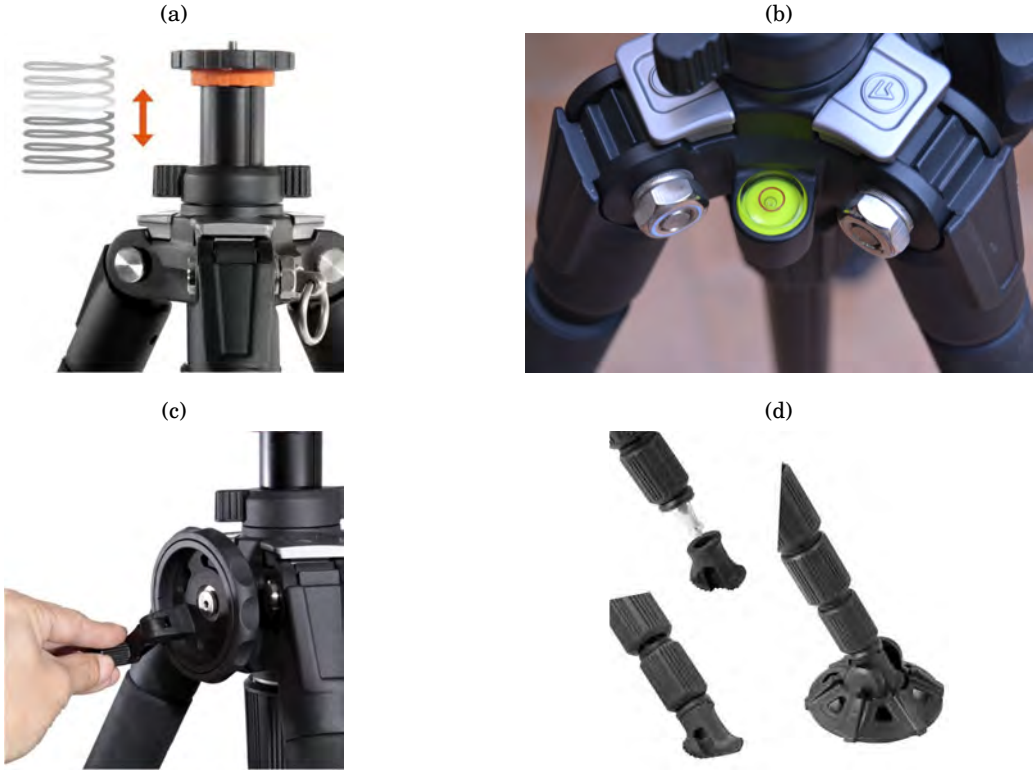

FIGURE 4.5. Detailed views of the weather station support [27]

4.2.2 Head

The main element of the weather station is the head. This is the one that holds the instrumentation required to obtain the wind velocity vector, and it rotates as a conventional weather vane. It is composed of two 3D printed parts (the tripod link and the top base) and a bearing that connects these two parts allowing the free movement in the vertical axis. Figure 4.6 shows the CAD model of the head.

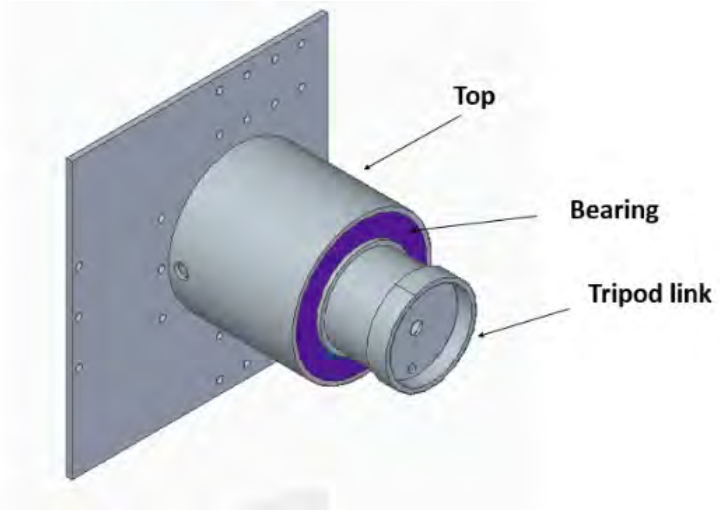

FIGURE 4.6. CAD model of the weather station head: Top, tripod link and bearing

.

4.2.2.1 Tripod Link

This element is aimed to join the head to the tripod. It is a cylindrical 3D printed part that fits in the interior face of a bearing. This part had to be completely fixed to the tripod head. As a first approach (Figure 4.7), a hole was included in its base in order to allow the screw thread to pass through it. It was meant to tighten the tripod link to the tripod base with a nut. However, this design was not stable enough so a reinforcement was included in the tripod link base (Figure 4.8). It allows the tripod link to fit into the tripod base, keeping fixed to it. Two more holes were also added just in case it was needed to screw the base to the link to reinforce the attachment.

4.2.2.2 Bearing

In order to allow the free movement about the vertical axis of the weather vane, a bearing was used. This part connects the tripod link to the head. The tripod link keeps motionless, but the head can rotate freely. The selection of the bearing was made focusing on the friction it may offer to the motion. The starting torque of the bearing, M_{start}, is the moment needed for the bearing to

FIGURE 4.7. CAD first model of the tripod link

FIGURE 4.8. CAD final model of the tripod link

start rotating and it is defined as follows [23]:

$$M_{start} = M_{SL} + M_{SEAL} \tag{4.2}$$

where M_{SL} is the sliding frictional moment and M_{SEAL} is the moment of the external shield in the case of a closed bearing as the one shown in Figure 4.9(a). Trying to avoid undesired friction, the selected bearing was an open deep groove ball 6012 one [Figure 4.9(b)]. Therefore $M_{SEAL} = 0$ in this case. The sliding frictional coefficient can be computed using the following expression:

$$M_{SL} = G_{SL}\mu_{SL} \tag{4.3}$$

where μ_{SL} is the sliding friction coefficient, that can be approximated to 0.095 for deep groove ball bearings, and G_{SL} is a sliding frictional variable depending on the axial and radial loads (F_a and F_r) supported by the bearing, its type and its mean diameter ($d_m = \frac{D+d}{2}$, see Figure 4.10). The axial load supported by the bearing can be considered as the total weight of the weather station's head with the instrumentation ($F_a = W = 5$ N). According to [23], since the axial load

supported by the bearing satisfies the following inequality:

$$F_a \leq 0.5C_0 \rightarrow 5N < 11.6 \text{ kN} \tag{4.4}$$

where C_0 is the basic static load rating, equal to 23.2 kN in this specific case; then the load can be considered pure axial and the parameter G_{SL} can be computed as:

$$G_{SL} = 3.73 \times 10^{-3} d_m^{-0.145} \left(14.60 d_m^{1.5} \times F_a^4\right)^{1/3} \tag{4.5}$$

Finally:

- G_{SL}=0.36 Nmm
- M_{start} = M_{SL}=0.034 Nmm

(a) (b)

FIGURE 4.9. Bearing with external shield (a) and final open bearing selected (b) [23]

(a) (b)

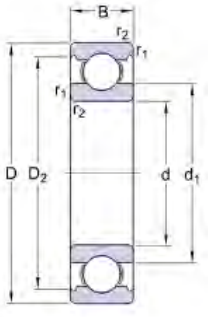

d		60	mm
D		95	mm
B		18	mm
d_1	≈	71.3	mm
D_2	≈	86.5	mm
$r_{1,2}$	min.	1.1	mm

FIGURE 4.10. Dimensions of the deep groove ball bearing used [23]

4.2.2.3 Top

The top of the weather station head is a 3D printed element aimed to support the airspeed sensor as well as the PixHawk with the compass. Therefore it has to rotate in order to provide the direction of the wind. That is the reason why this element is joint to the bearing, being the last one fitted in its interior (Figure 4.6).

This part is composed of a hollow cylindrical base which is joint to the bearing and a rectangular head that holds the instrumentation. Several through-the-thickness holes have been included in the head. They are meant to be used to hold some instruments with bridles, either now or in the future. A transversal hole was also created in the cylindrical base in order to pass the weather vane bar through them. Figure 4.11 shows two views of the CAD model of this element.

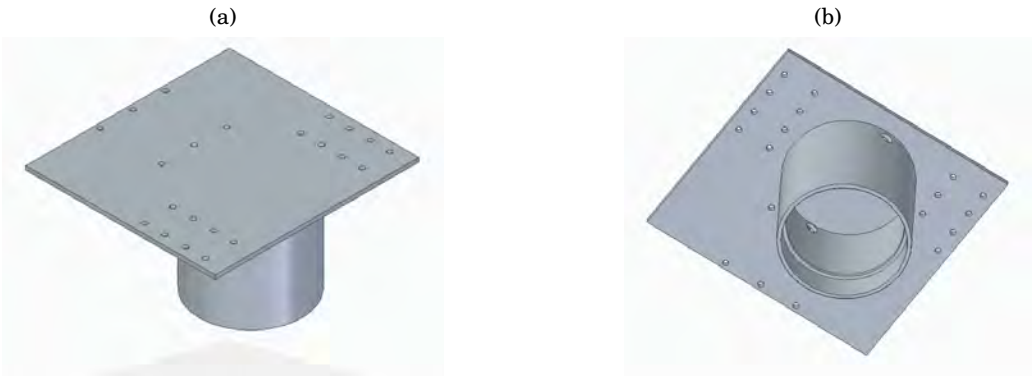

FIGURE 4.11. CAD model of the top head

4.2.3 Weather Vane Arrow

The weather vane arrow (Figure 4.12) is the element that holds the Pitot sensor on the one hand, and provides the torque needed for the weather station head to rotate. It is composed of three elements:

4.2.3.1 Aluminium Bar

A typical weather vane requires to have an arrow that freely rotates being aligned with the wind. In this case a hollow aluminium bar was chosen to be the body of this arrow. It has an external diameter of 10 mm and an internal one of 8 mm. The material of the bar was chosen to be aluminium due to its stiffness and lightness. The length of the bar is 880 mm, more than enough to provide a torque around the vertical axis of the weather station.

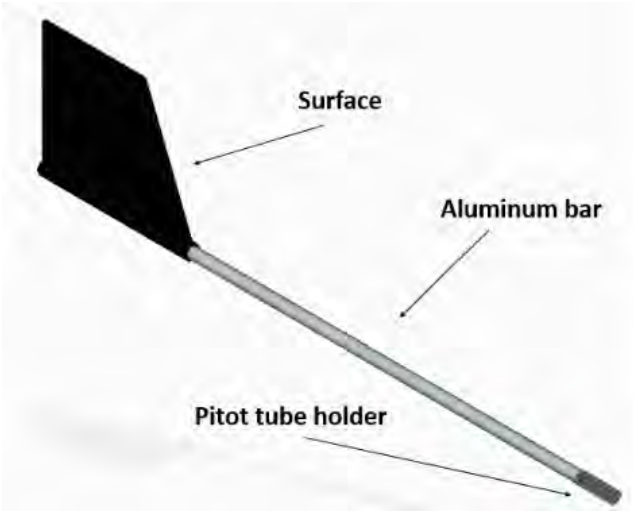

FIGURE 4.12. CAD model of the weather vane arrow

.

4.2.3.2 Pitot Tube Holder

The Pitot tube holder is an element that grabs the Pitot tube to the aluminium bar. It is a 3D printed part with a cylindrical shape that fits in the front part of the aluminium bar. As a first approach, the Pitot tube was thought to be fitted in a smaller hollow cylinder in the upper part of the holder [Figure 5.8(a)]. However, in order to pass the tube through the cylinder, the diameter of the last one had to be slightly bigger than that of the tube and the tube was wobbly, which is not desired. Therefore, the configuration in Figure 5.8(b) was finally chosen.

FIGURE 4.13. CAD model of the Pitot holder. First attemp (left) and final model (right)

4.2.3.3 Tail Surface

The remaining element of the weather vane arrow is the surface located at its tail. In this case, in order to adapt it to the aluminium bar, the surface was made making use of 3D printing. It consists of a hollow cylinder with internal diameter equal to the external one of the bar, which is extended in a rectangular-trapezium shape of surface S=0.02 m^2 (surface which is hit by the wind).

4.2.3.4 Minimum wind speed required to move the station

It is interesting to know how sensible to the wind speed the weather station is. In section 4.2.2.2 the minimum torque needed to rotate the station was computed. Knowing this data the minimum wind speed required to do so can be estimated using Equation 4.1. It will be considered that $\vec{r}$ will be the arm of the weather vane whose norm will be selected to be r = 700 mm and $\vec{F}$ the drag force offered by the tail surface, whose magnitude is expressed in the following way:

$$F = \frac{1}{2}\rho V_w^2 S C_D \tag{4.6}$$

where ρ is the density of the air, S the surface of the tail and C_D the corresponding drag coefficient.

Substituting M_{start} and the arm of the weather vane in Equation 4.1, the minimum force required to move the weather station (F_{min}) will be:

$$F_{min} = \frac{M_{start}}{r} = 4.9 \times 10^{-5} \text{ N} \tag{4.7}$$

Solving for the wind speed in Equation 4.6, the result is:

$$V_{w,min} = \sqrt{\frac{2F_{min}}{S\rho C_D}} = 0.06\text{m/s} \tag{4.8}$$

where ρ = 1.16kg/m^3 considering an altitude of 680 m, C_D=1.28 [22] and S=0.02 m^2

4.2.4 Instrumentation

Finally, some instruments were needed to measure the wind velocity. The UC3M research group had already some instrumentation that was thought to be used for the purpose of this project. Therefore the design of the weather station was carried out taking into account the integration of these instruments at all times.

The mentioned devices are: a Pitot tube with an airspeed sensor to measure the wind speed, a magnetometer to provide the direction of the wind and finally a Pixhawk autopilot connected to both sensors previously mentioned, which was used as a data logger. It has been taken into account that the kites are already provided with a Pixhawk controller thus the process of data obtaining from them and from the station will be homogeneous and will be logged with the same time interval. This is really important since data from both elements will have to be combined in order to compute the aerodynamic velocity of the kites in future projects.

4.2.4.1 Pixhawk

The Pixhawk autopilot is a high-performance controller which is currently used in many UAV's applications, either in the amateur or industrial communities due to its versatility and low cost. It is part of the Pixhawk project, an independent, open-hardware initiative.

This autopilot has many applications which are beyond the scope of this project, for which it will be used as a data logger only, providing homogeneity to the data obtaining process. In fact, it is provided with some integrated inertial sensors that constitute two Inertial Measurement Units (IMU) that allow it to measure velocity, acceleration and gravitational forces of the body. These sensors are:

- ST Micro L3GD20 3-axis 16-bit gyroscope.
- ST Micro LSM303D 3-axis 14-bit accelerometer/magnetometer.
- Invensense MPU 6000 3-axis accelerometer/magnetometer.
- MEAS MS5611 barometer.

The reason why it has two IMUs is due to this controller is normally used in many types of flying devices and reliability and safety are paramount issues to be taken into account.

On the other hand the Pixhawk is provided with several ports corresponding to different elements depending on the function it will perform. In this case it will be connected to an external compass and to an airspeed sensor. Moreover, it will also have to be fed by a power supply device composed of four batteries. Figure 4.14 shows an image of the Pixhawk controller used in this project. It is important to mention that the firmware that will be used to control the Pixhawk is the open-software PX4.

FIGURE 4.14. Pixhawk

.

4.2.4.2 Pixhawk Airspeed Sensor Kit

In order to measure the wind speed a digital airspeed sensor connected to a Pitot tube will be used. This Pixhawk Airspeed Sensor Kit [Figure 4.16(a)] is provided with:

- A **Pitot tube** to measure static and total pressure.

  An example of a Pitot tube is shown in Figure 4.15. It consists of a tube with several holes drilled around its outside part and a center hole drilled down the axis of the tube. The outside holes are perpendicular to the direction of the wind so they measure the local random component of the air velocity. The pressure in these small tubes is the static one (P_s). On the other hand, the center hole in the tube points to the direction of the wind and is affected by both the random and the ordered air speed [60]. Therefore the pressure in this tube is the total one (P_t).

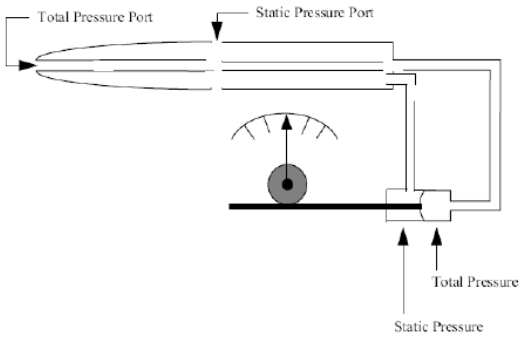

FIGURE 4.15. Pitot tube fundamentals. Figure from [53].

- A **digital airspeed sensor** to obtain the indicated airspeed (IAS), provided with a Measurement Specialities 4525DO Digital Pressure Transducer [Figure 4.16(b)] with the following characteristics [16]:

  - Pressure difference range (Full Scale): up to 1 psi (6894.76 Pa)
  - Airspeed range: up to 100 m/s
  - Digital resolution: 0.84 Pa
  - Accuracy (error in the measurements): ± 0.25% FS (Full Scale).
  - 14 bit Analog to digital converter (ADC)

  This pressure transducer is connected to the Pitot tube and therefore it has two inputs, P_s and P_t. It measures the difference between these two pressures leading to the dynamic pressure, according to Bernoulli's equation:

$$P_s - P_t = \frac{1}{2}\rho V_w^2 \tag{4.9}$$

This equation can be used to obtain the indicated airspeed (IAS) if the flow is incompressible ($M_\infty < 1$), which is the case of the weather station application. The maximum wind speed (V_w) expected below 30 m above ground level (where UC3M kites will fly) is approximately 10 m/s [40], whereas the sound speed (a) can be approximated to 337.65 m/s. Therefore, the expected Mach number will be:

$$M_\infty = \frac{V_w}{a} \leqslant 0.03 \tag{4.10}$$

The indicated airspeed is obtained applying the following equation [53]:

$$V_{w,IAS} = \sqrt{\frac{P_s - P_t}{\frac{1}{2}\rho}} \tag{4.11}$$

Since there are no compressibility effects, this speed can be considered equal to the equivalent airspeed (EAS). The MS5611 Barometric Pressure Sensor on the Pixhawk allows to calculate the true airspeed from the equivalent airspeed. It has a built-in temperature sensor which is used to correct the density variations that may appear. The true airspeed is obtained as follows [53]:

$$V_{w,TAS} = \frac{V_{w,EAS}}{\sqrt{\sigma}} \tag{4.12}$$

where σ is the ratio between the density at the point where measurements are taken (ρ) and the density at sea level (ρ_0):

$$\sigma = \frac{\rho}{\rho_0} = \theta^{4.2561} \tag{4.13}$$

This ratio is related to θ, the quotient between the temperature at the point of the measurements (T) and the one at sea level (T_0):

$$\theta = \frac{T}{T_0} \tag{4.14}$$

- Two **rubber tubes** to connect the Pitot tube outputs (P_s and P_t) to the airspeed sensor.
- I^2C (***Inter-Integrated Circuit***) **cabling** to connect the airspeed sensor to the Pixhawk.

(a) (b)

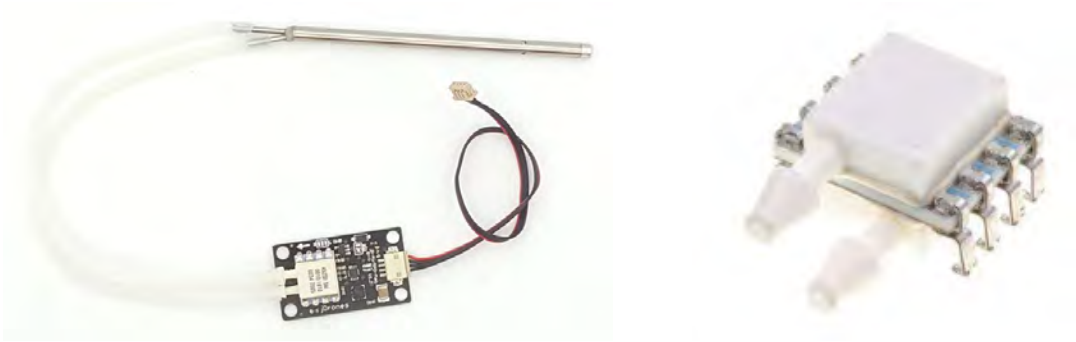

FIGURE 4.16. Pixhawk Airspeed Sensor Kit (a) and pressure transducer embedded in the airspeed sensor (b)

4.2.4.3 3DR uBlox GPS with Compass Kit

The direction of the wind velocity will be obtained making use of a magnetometer. Magnetometers are widely used in the navigation environment to know te heading of a vehicle. In this case, positioning a magnetometer pointing to the direction the wind is coming from, the heading of the weather station and therefore the orientation of the wind can be obtained.

In this case a 3DR module that incorporates a GPS and a compass will be used. The reason why an external magnetometer has been chosen instead of using the internal ones of the Pixhawk is because this one provides more accuracy in the measurements. Moreover it is combined with a GPS that allows to know the exact position of the weather station when tests are performed.

The magnetometer included in the module is a HMC5883L three axis digital compass with the following specifications [1]:

- Magnetic field range: ± 8 Gauss
- Compass heading accuracy: ± 1-2 °
- Resolution: 2 milli-Gauss.
- 12 bit Analog to digital converter (ADC)

Communication with the HMC5883L is simple and all done through an I^2C interface. Figure 4.17 shows the module with the integrated compass and the corresponding I^2C cabling to allow the connexion between the module and the Pixhawk.

4.2.4.4 I^2C splitter

The I^2C splitter allows to connect multiple peripherals to the Pixhawk I2C port; in this case the digital airspeed sensor and the external compass.

FIGURE 4.17. 3DR uBlox GPS with Compass Kit

.

FIGURE 4.18. I^2C splitter

.

CHAPTER 5

WEATHER STATION IMPLEMENTATION

This chapter explains how the elements of the system are interconnected to work together providing the final objective. It shows the assembly of the whole weather station as well as the set-up process carried out in order to calibrate the instrumentation before the testing phase.

5.1 Assembly of the system

5.1.1 Head elements assembly

The head of the weather station is composed of three main elements: the top part, the bearing and the tripod link. The top and the tripod link were designed according to the dimensions of the bearing thus fitting perfectly. These three parts do not require any type of adhesive being just fitted together. Both the top and the tripod link have a protuberance in order to act as limits for the bearing. In Figure 5.1 the assembly of the head elements can be seen.

5.1.2 Head-support assembly

The head is joined to the tripod by means of the tripod link. This part fits in the tripod head being the base external diameter equal to the tripod link internal one. Again, there is no need of adhesive to join tightly these two elements. As shown in Figure 5.2 the screw thread of the tripod head passes through the central hole of the tripod link. Since the two parts are fitted, there is no need of screwing the base to the link using the two back-up screws provided in the tripod head.

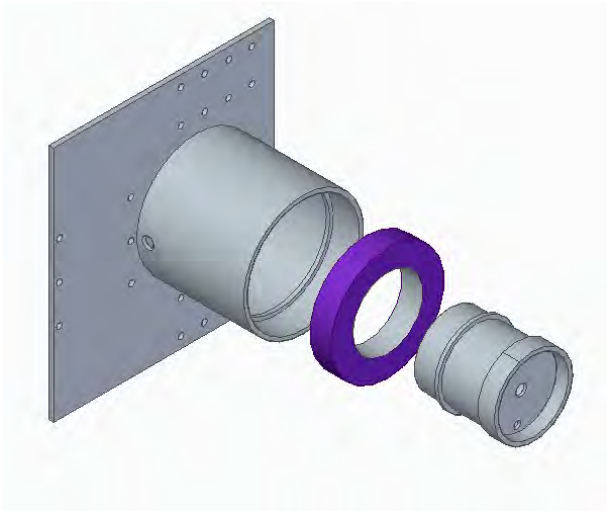

FIGURE 5.1. Head elements assembly

(a) (b)

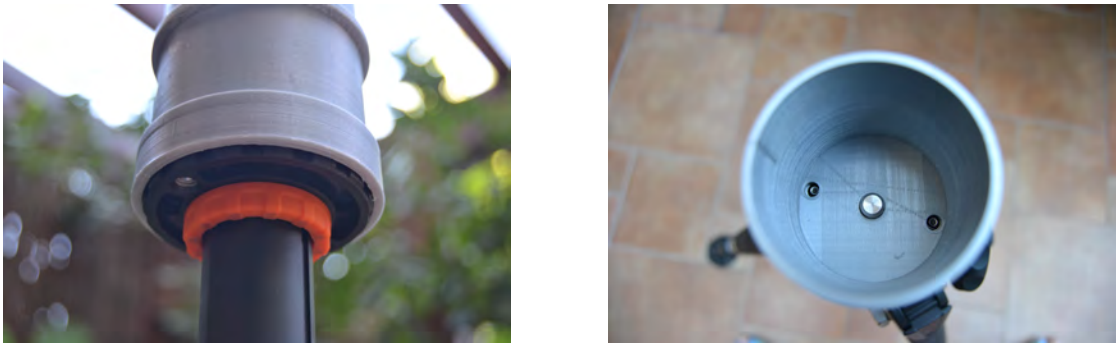

FIGURE 5.2. Head-support assembly

5.1.3 Weather Vane Arrow assembly

Regarding the assembly of the weather vane arrow elements, it follows the same philosophy used in the previous assemblies. The Pitot tube holder fits in the aluminium bar [Figures 5.3(c)-5.3(d)] and the bar fits in the surface located at its tail [Figure 5.3(a)]. Since the surface has to keep straight, in this case the bar was covered with insulating tape in order to tighten the fitting of the surface and avoid it to rotate around the bar due to its own weight. On the other hand, the aluminium bar is fitted in the top part of the weather station head passing through the holes included in the cylindrical part [Figure 5.3(b)].

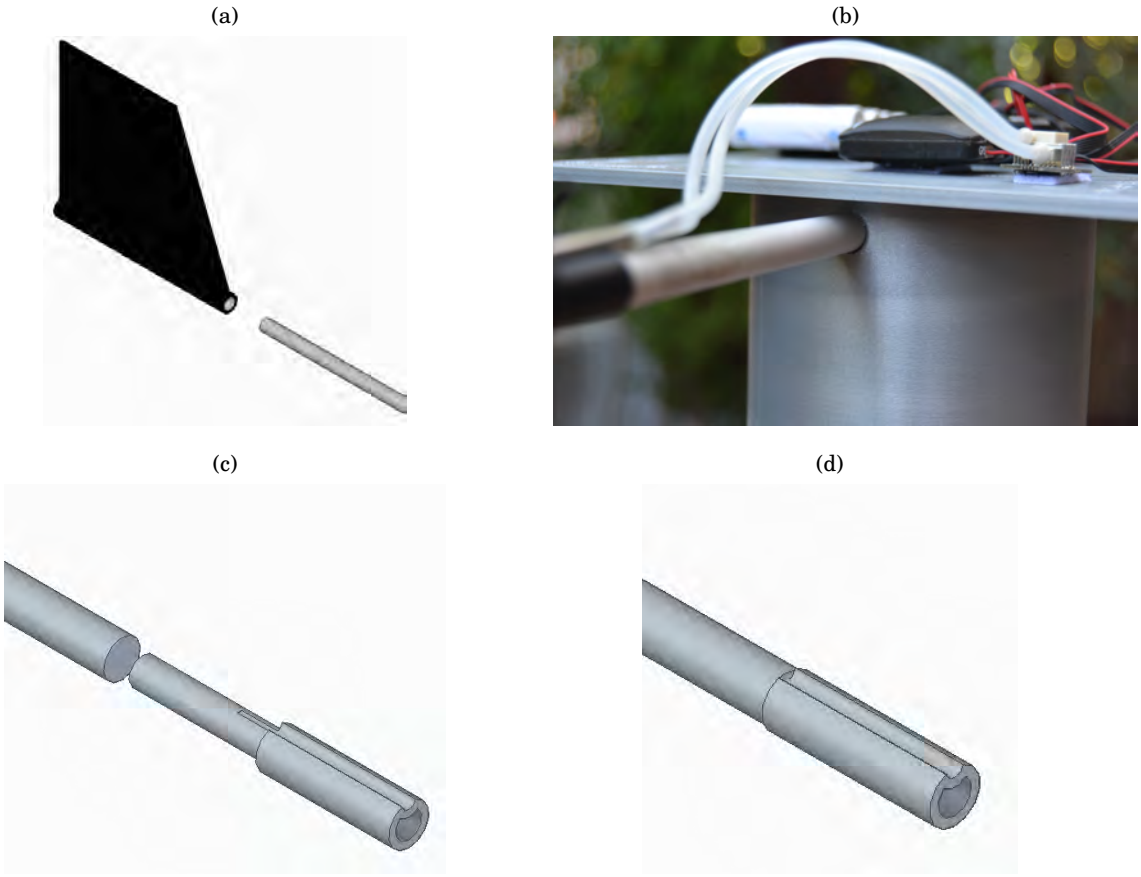

FIGURE 5.3. Weather Vane Arrow assemblies

5.1.4 Instrumentation assembly

Figure 5.4 shows the CAD model of the assembled weather station highlighting the location of the required instrumentation. In general, the instruments are attached to the weather station head with Velcro. This is the case of the Pixhawk power supply, the magnetometer, the I2C splitter module and the airspeed sensor [Figure 5.5(b)]. On the other hand, the Pixhawk is attached with two bridles [Figure 5.5(a)] passing through the holes provided in the top of the weather station head.

Finally, the Pitot tube is located in the cylindrical slot on the top of the Pitot holder. The motion of the tube is avoided with the aid of a bridle [Figure 5.5(c)].

5.2 Instrumentation inter-connexion

In order to work, the sensors have to be connected to the Pixhawk autopilot which in turn has to be fed by the power supply module. The communication between the sensors (airspeed sensor and compass) with the Pixhawk autopilot will be made through I^2C (Inter-Integrated Circuit)

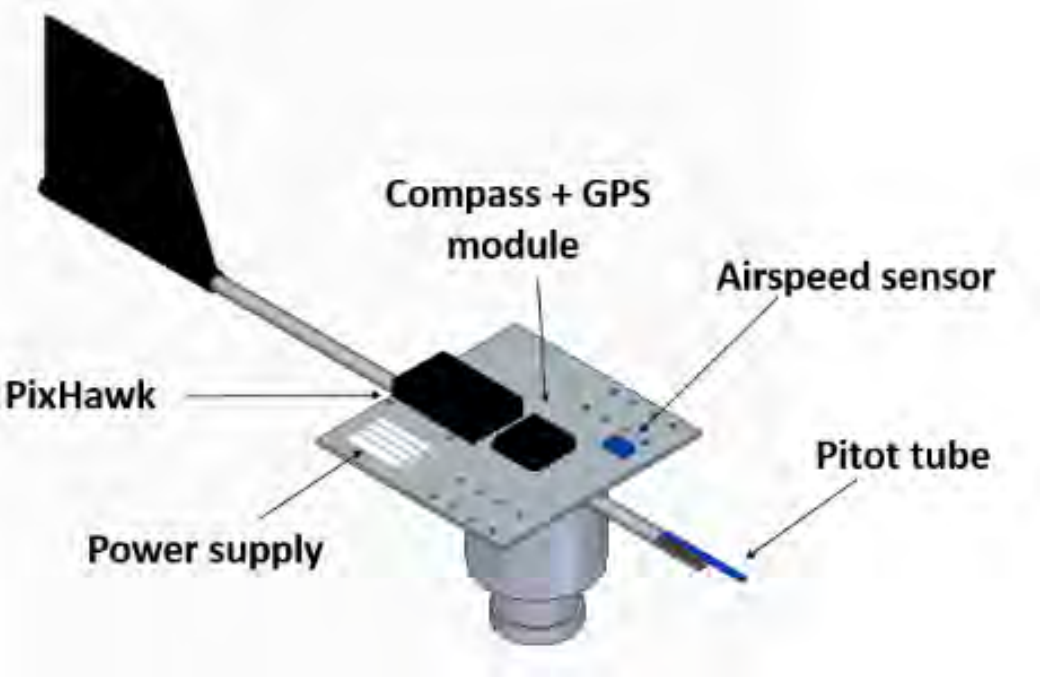

FIGURE 5.4. CAD model with the location of instrumentation in the weather station.

.

buses. I^2C connection is normally used for attaching lower-speed peripheral IC's (Integrated Circuits) to processors and microcontrollers in short-distance. The Pixhawk controller has a I^2C port that allows this kind of connexion. However, in order to connect more than one peripheral device as it is the case, a I^2C splitter module is needed. This module acts as a bridge between the peripherals (airspeed sensor and compass) and the Pixhawk controller. Connexions are made with four-position DF13 cables. The GPS of the 3DR ublox module is connected to the GPS port in the Pixhawk. Figure 5.7 shows the connexion between the sensors and the Pixhawk controller in the real weather station model. Moreover, a schematic explanation is provided in Figure 5.6.

Regarding the connexion between the Pitot tube and the airspeed sensor, it is made through two rubber tubes which connect each of the input sensor cones to the corresponding output extension of the Pitot tube. The tube attached to the cone on the top airspeed sensor board is connected to longer extension of the Pitot tube. On the other hand, the shorter extension of the Pitot tube is connected to the cone protruding from the base of the board. This is shown in Figure 5.8.

5.3 Instrumentation set-up and calibration

It is paramount to know the accuracy and quality of the measurements recorded before testing a system. The goal of the calibration process is to define these parameters allowing to quantify and

(a)

(b)

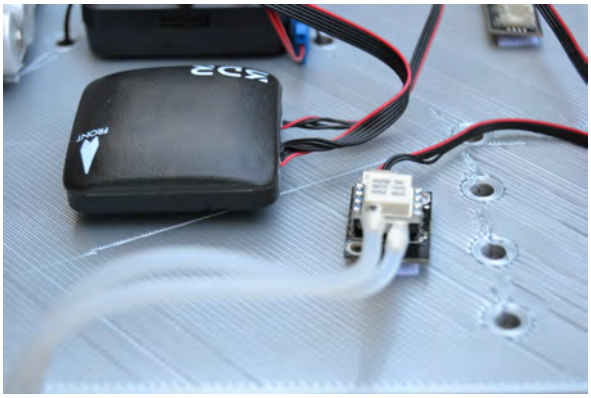

(c)

FIGURE 5.5. Instrumentation assembly

control errors or uncertainties that may appear in the measurements.

In order to set-up the sensors used in the weather station different procedures have been followed. On the one hand, some issues such as the orientation of the Pixhawk have been configured using Qgroundcontrol, an open-source platform that "provides full flight control, mission planning and complete set-up/configuration for PX4 or ArduPilot powered vehicles" [19]. On the other hand, an *ad hoc* process has been derived in order to calibrate the external compass since Qgroundcontrol requires the Pixhawk to be connected to the computer and this device may be a perturbing element in the magnetic field. Finally, the accuracy of the airspeed sensor has been proven making a calibration with the aid of a wind tunnel.

5.3.1 Qgroundcontrol

Among the wide range of uses this platform offers, it will be used to set-up the local horizon and the orientation of the Pixhawk and magnetometer. In order to work properly, the accelerometer and gyroscope will be also configured although they will not be needed for the purpose of this

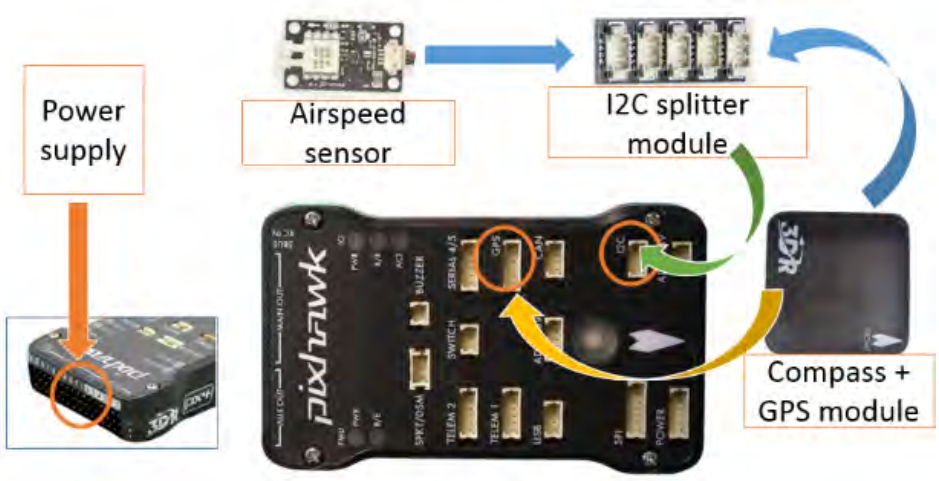

FIGURE 5.6. Sensors-Pixhawk connexions

.

FIGURE 5.7. Connexion between the instruments of the weather station.

.

thesis. Figure 5.10 shows the Qgroundcontrol environment. The tab 'sensors' will be the relevant one for the set-up process.

In order to carry out the process, the Pixhawk is connected to the computer via USB. After that the Pixhawk looks for GPS signal (meanwhile its LED becomes blue) and once it is found (the LED becomes green), the configuration can be started.

To level the horizon, the Pixhawk has to be positioned in the level position it will have during the tests; it means, in the top of the weather station. To assure the station is perfectly horizontal, the tripod bullseye level should be used. Then, to set the orientation of the external compass and

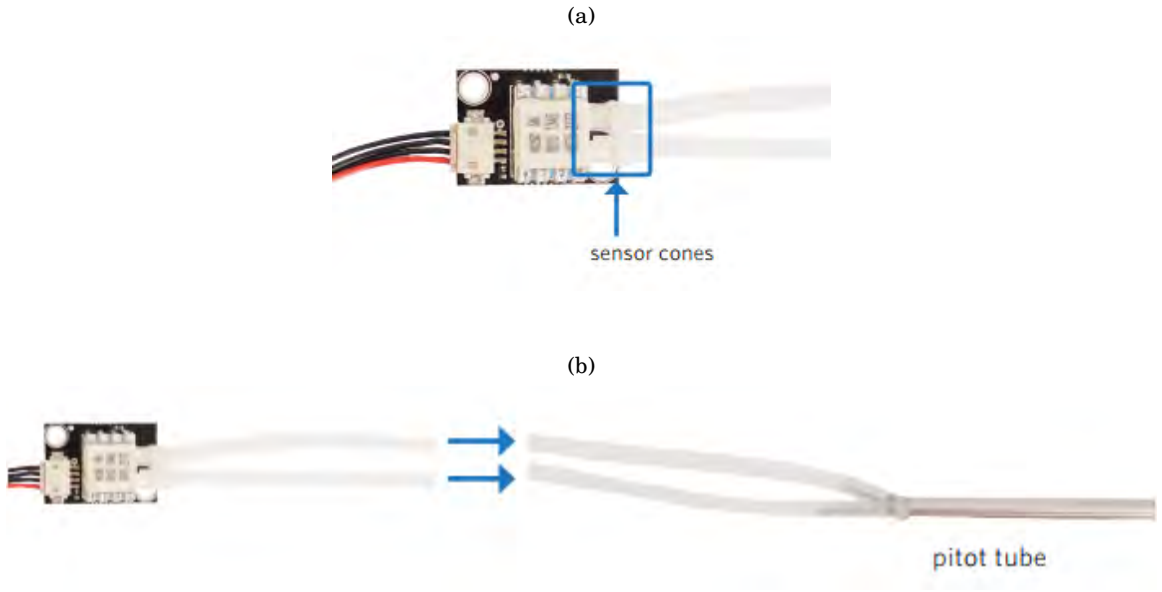

FIGURE 5.8. Pitot tube-airspeed sensor connexions

the Pixhawk itself, they have to be positioned in the orientation of flight: both with the white arrow looking forward in the direction the wind is coming from. Figure 5.9 shows graphically how the sensors should be oriented. With this orientation, the reference frame used by the Pixhawk is the body axes one typically used in aviation with the x pointing toward the front of the weather station facing the wind, the y axis pointing to the right of the station and the z axis pointing downwards.

5.3.2 Magnetometer Calibration

Although Qgroundcontrol is able of calibrating magnetometers, it requires the sensor to be near the computer, which can be a source of perturbation in the magnetic field. Moreover, the weather station has some sources of own perturbation such as the bearing and some screws contained in the tripod. Therefore, the magnetic field measured by the magnetometer may suffer from disturbances that have to be taken into account.

The methodology used in the compass calibration is based on the one described in [51]. Its objective is to correct the measurement errors once the measurements have been taken. In order to do that, the magnetic field obtained by the magnetometer will be modified taking into account these perturbations.

5.3.2.1 Earth's Magnetic Field

The Earth's magnetic field can be considered as a vector ($\vec{B}$) defined by three components: B_x,B_y and B_z:

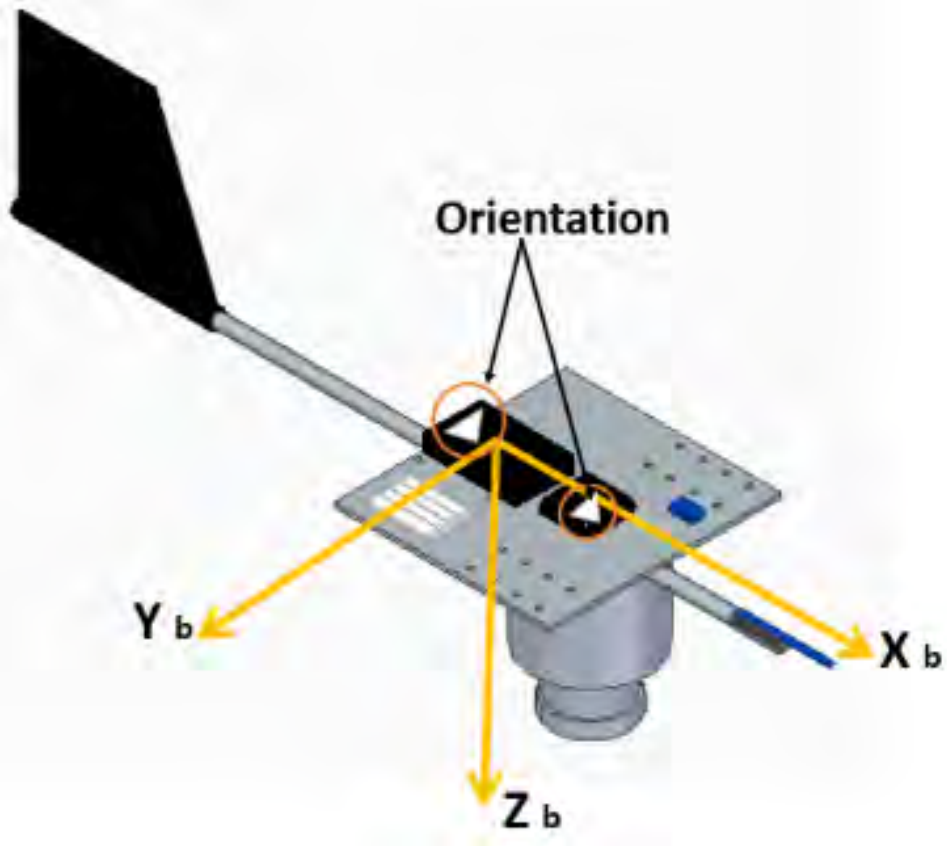

FIGURE 5.9. Sensors orientation and body axes reference frame used by the Pixhawk.

.

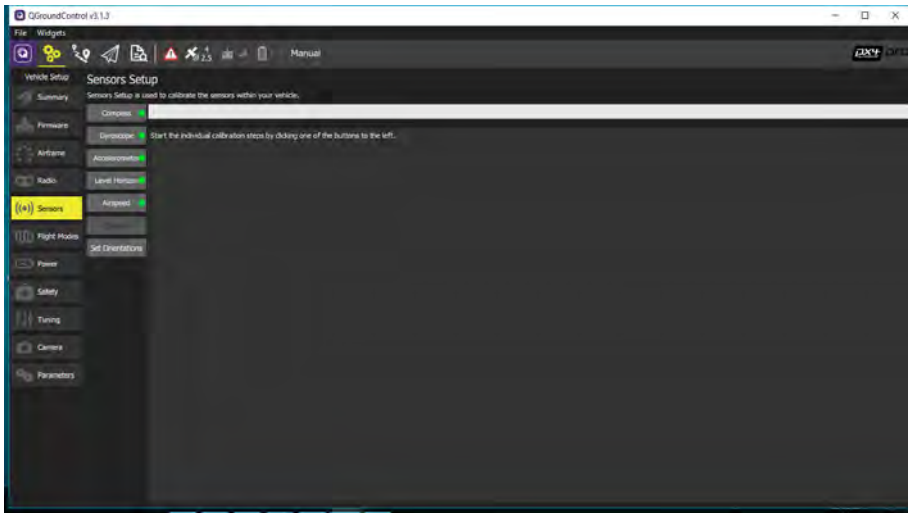

FIGURE 5.10. Qgroundcontrol environment.

.

$$\vec{B} = [B_x, B_y, B_z]^T \tag{5.1}$$

This field is usually defined in the North-East-Down (NED) frame of reference (Figure 5.11), whose x axis is pointing to the true geographic North, y in the East direction and z pointing downwards. It exists a discrepancy between the True North (the one that points towards the geographic North Pole) and the magnetic north (the one given by a compass). The second one, which can be considered as the heading $\vec{H}$ of the magnetometer (determined by the B_x and B_y components of the magnetic field, see Figure 5.11), is usually affected by a declination angle D with respect to the True North. This declination depends on the latitude and longitude of the point where the measurements are taken. In the case of Leganés (where tests have been carried out), the declination angle is approximately 0° [13]. Therefore in this case, the heading of the compass would coincide with the true geographic North.

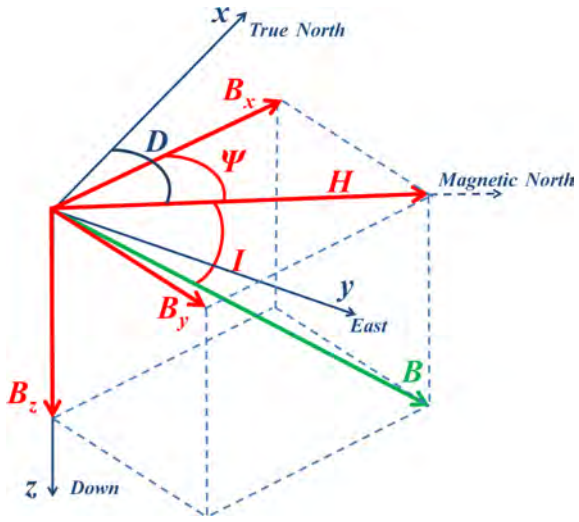

FIGURE 5.11. Earth's magnetic field in NED coordinates. Figure from [35]

.

On the other hand, the magnetometer of the weather station uses the same frame of reference as the Pixhawk. Therefore it measures the magnetic field given in the body axes normally used in Flight Mechanics, where X_b is facing the wind in this case, Y_b is in the horizontal plane of the weather station, parallel to the Earth's surface (assuming no pitch nor roll, since the weather station must be perfectly horizontal in order to give accurate results) perpendicular to the previous axis and Z_b points downwards. In these coordinates the wind is said to be in $-\vec{i}_b$ direction (see Figure 5.12). Since the compass determines the magnetic field in these body axes and the True North coincides with the magnetic North (heading of the compass, $\vec{H}$) then the direction of the wind can be known computing the angle between the North and the heading of the weather station (X_b axis). This angle is going to be called ψ or heading angle. Figure 5.13

shows more clearly this concept. The compass defines the magnetic field $\vec{B}_b$ in the components $B_{x,b}$, $B_{y,b}$ and $B_{z,b}$, where the subscript b means that they are expressed in body axes:

$$\vec{B}_b = B_{x,b}\vec{i}_b + B_{y,b}\vec{j}_b + B_{z,b}\vec{k}_b \tag{5.2}$$

To know the wind direction, only the components that determine the heading ($\vec{H}_b$) of the compass are relevant. The compass heading can be defined as:

$$\vec{H}_b = B_{x,b}\vec{i}_b + B_{y,b}\vec{j}_b \tag{5.3}$$

where $B_{x,b}$ and $B_{y,b}$ are the components of the magnetic field projected in X_b and Y_b (see Figure 5.13). The heading angle ψ can be computed knowing their values.

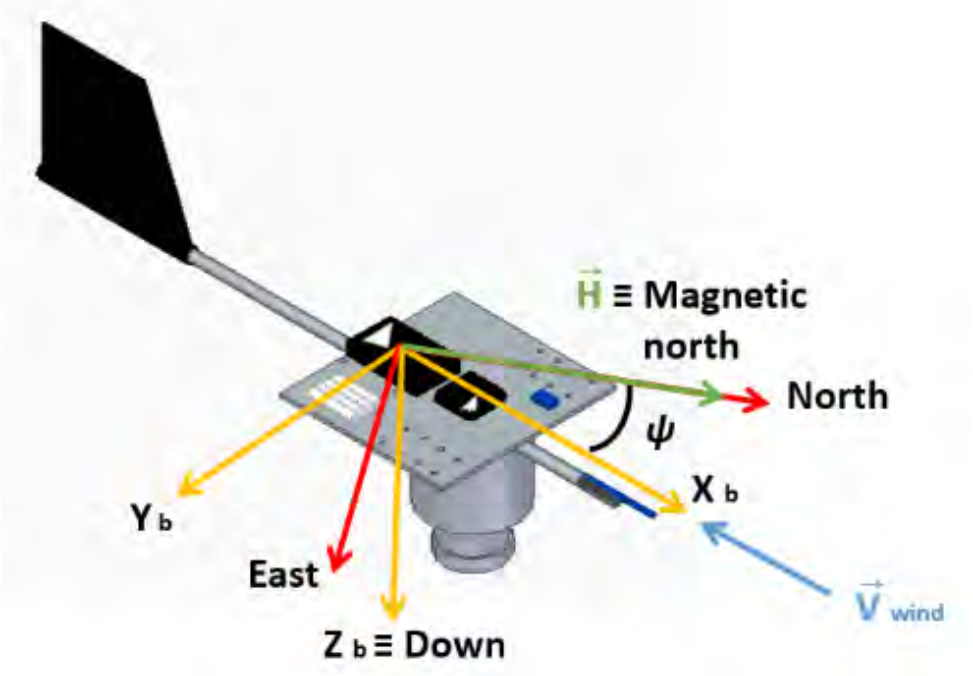

FIGURE 5.12. NED and body axis reference frames in the weather station. The North-East and the X_bY_b planes coincide with the horizontal plane of the weather station, which is parallel to the Earth's surface. Angle ψ determines the heading of the weather station and therefore the direction of the wind.

The total intensity of the Earth's magnetic field (the magnitude of the vector $\vec{B}$), usually measured in Gauss or Tesla, depends on the location of the point where the field is measured. Its value is in the range between 0.25 Gauss (in the magnetic Equator) and 0.60 Gauss (at the magnetic Pole) [14]. The horizontal intensity of the magnetic field (the magnitude of the vector $\vec{H}$) is another useful variable. Of course, this parameter also depends on the location of the point where the field is measured. If a compass reads the magnetic field at one determined point, the heading vector will have always the same magnitude regardless of the orientation of the compass.

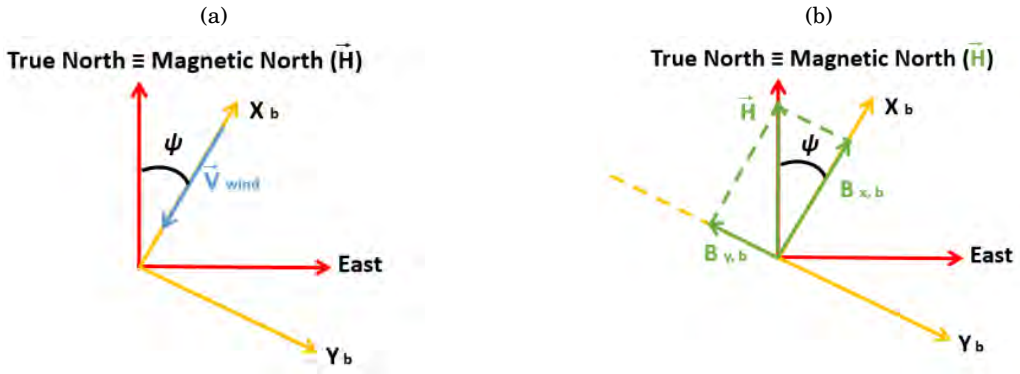

FIGURE 5.13. Earth's magnetic field in body axes

If the magnetometer is positioned horizontally (parallel to the Earth's surface) and it is rotated 360 °, all possible vectors $\vec{H}$ will describe a circle with radius equal to the horizontal intensity of the magnetic field at the point where it is located. For example in Leganés this magnitude is approximately equal to 0.256 Gauss (value estimated using the Matlab function *wrldmagm.m* [29]). Thus the horizontal magnetic field in this city will be the one shown in Figure 5.14 for all possible compass orientations.

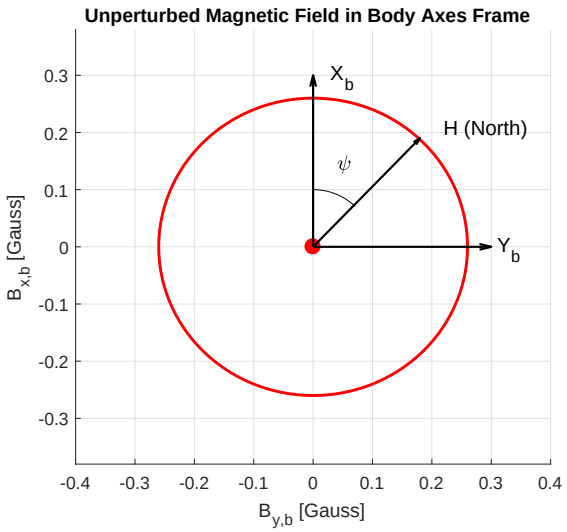

FIGURE 5.14. Unperturbed Earth's magnetic field in body axes

5.3.2.2 Characteristics of the Compass Calibration Test

The magnetic field shown in the previous section is the one generated by the Earth without any perturbation. However, magnetometers may be disturbed by some interferences in their vicinity that may perturb their measurements. During the magnetometer calibration test, the

weather station was positioned in a park in the city of Leganés. The place has the following characteristics:

- Latitude: 40 °19' N
- Longitude: 3 ° 47' W
- Altitude: 680 m
- Magnetic declination (D): -0° 40' (Negative: West)
- Total magnetic field intensity (B): 0.447 Gauss
- Horizontal magnetic field intensity (H): 0.256 Gauss

The magnetic field measured after rotating the weather station 360 ° differed a little from the expected unperturbed one, as shown in Figure 5.15. It can be observed how the measured field is a bit displaced from the centre of the reference frame and how it is not a perfect circumference. This is due to the perturbations affecting the magnetic field, which can be classified into two groups: hard iron and soft iron interferences [51].

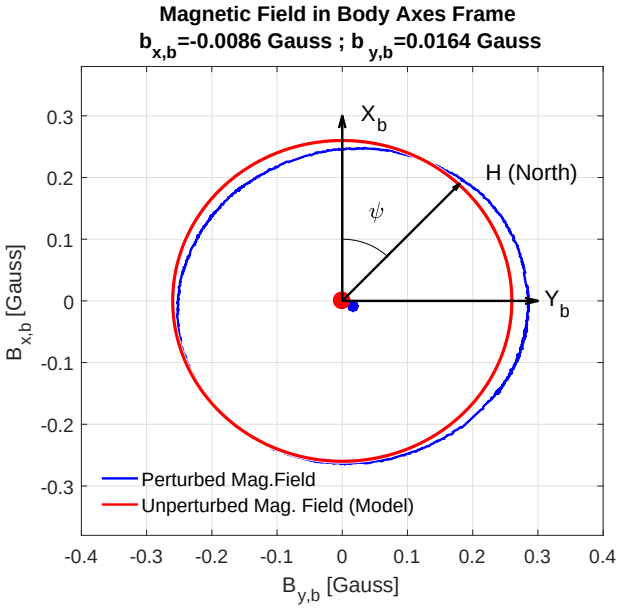

FIGURE 5.15. Comparison between unperturbed Earth's magnetic field and measured field in body axes

5.3.2.3 Hard Iron Interferences

The first group includes constant or slowly time-varying fields produced by ferromagnetic materials close to the magnetometer. The measurement errors resulting from these interferences are

known as hard iron bias, and they generate a constant additive value to one or more magnetic field components shifting the centre away from the origin [Figure 5.16(a), red]. A vector $\vec{b}_b$ whose components are the hard iron bias in X_b and Y_b directions is added to the unperturbed magnetic field (Equation 5.7). The resulting perturbed field will be defined as:

$$\vec{B}_{b,perturbed} = \vec{B}_b + \vec{b}_b = [B_{x,b}, B_{y,b}]^T + [b_{x,b}, b_{y,b}]^T \tag{5.4}$$

The components of the hard iron interferences are simply the offsets in X_b and Y_b axis of the magnetic field with respect to the centre of coordinates (unperturbed field). They are computed calculating the mean value of the maximum and minimum values of the perturbed magnetic field in the corresponding axis [see Figure 5.16(b)], as equations 5.5 and 5.6 indicate.

$$b_{x,b} = \frac{B_{x,b_{max-perturbed}} + B_{x,b_{min-perturbed}}}{2} \tag{5.5}$$

$$b_{y,b} = \frac{B_{y,b_{max-perturbed}} + B_{y,b_{min-perturbed}}}{2} \tag{5.6}$$

The hard iron bias measured during the calibration test were: $b_{x,b}$=-0.0086 Gauss and $b_{y,b}$=0.0164 Gauss.

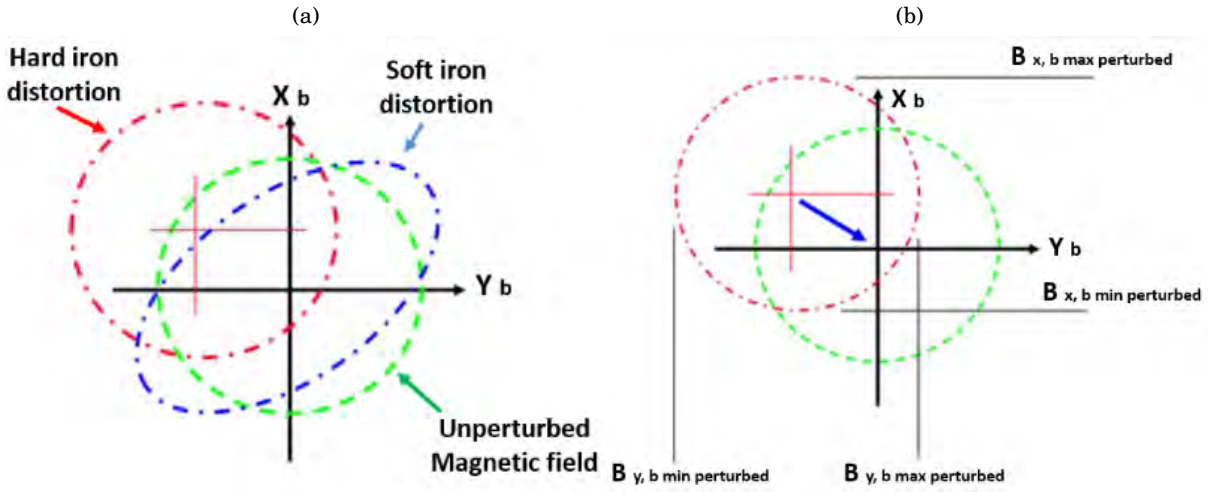

FIGURE 5.16. Hard iron and soft iron bias. Figures from [10]

5.3.2.4 Soft Iron Interferences

The second source of perturbations in the magnetic field is due to some materials that generate their own magnetic field in response to an external field applied. These errors produce a distortion in the shape of the magnetic field, that becomes an ellipse [Figure 5.16(a), blue] of eccentricity e.

5.3.2.5 Correction of Hard Iron Interferences

As shown in Figure 5.15, the soft iron interferences in the measurements are very small since the measured field has a small eccentricity (e=0.3, where e=0 is a circle). Therefore it was decided to correct first the hard iron perturbation in order to see how this correction affected the accuracy of the measurements. These perturbations were corrected subtracting the corresponding bias in each axis to the measured magnetic field:

$$\vec{B}_{\text{b, corrected}} = \vec{B}_{\text{b, perturbed}} - \vec{b}_{\text{b}} = [B_{\text{x,b perturbed}}, B_{\text{y,b perturbed}}]^T - [b_{\text{x,b}}, b_{\text{y,b}}]^T \tag{5.7}$$

Results are given in Figure 5.17. It can be observed that the hard iron corrected field, already centred at the origin, is practically a circle, leading to the conclusion of negligible soft iron interferences. Therefore, soft iron is definitely not worth being corrected.

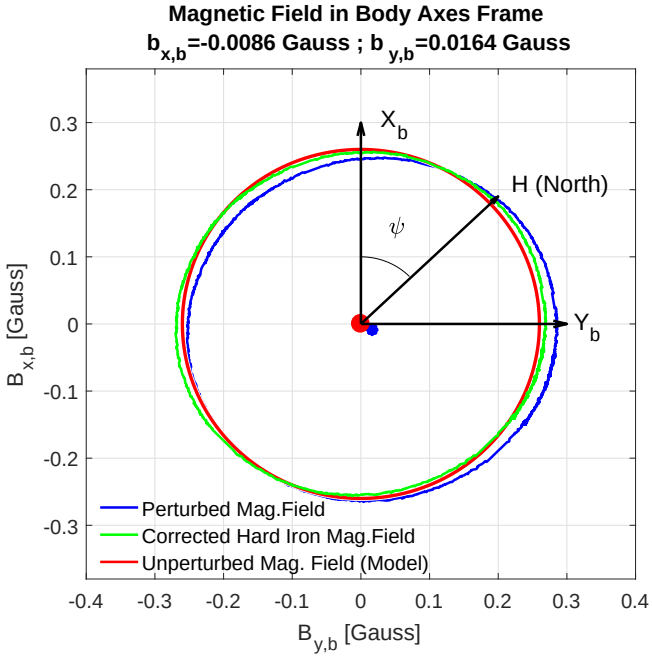

FIGURE 5.17. Comparison between unperturbed Earth's magnetic field and measured field in body axes before and after hard iron bias correction

In order to see if the hard iron should be corrected in future measurements, the heading of the weather station has been computed (Equation 5.8, [6]) using the raw perturbed magnetic field and the hard iron corrected one.

$$
\begin{aligned}
y = 0 \;;\; x > 0 \quad &\rightarrow \quad \psi = 0° \\
y = 0 \;;\; x < 0 \quad &\rightarrow \quad \psi = 180° \\
y < 0 \quad &\rightarrow \quad \psi = 270 - \arctan\left(\frac{x}{y}\right)\frac{180°}{\pi} \\
y > 0 \quad &\rightarrow \quad \psi = 90 - \arctan\left(\frac{x}{y}\right)\frac{180°}{\pi}
\end{aligned} \tag{5.8}
$$

Results are shown in Figures 5.18 and 5.19. It can be observed that practically no difference appears. Therefore, in future measurements there would not be an appreciable difference between obtaining the wind direction using the raw magnetic field or the corrected one. The error in the heading measurements will be determined by the accuracy of the magnetometer used, in this case from 1° to 2 ° [1].

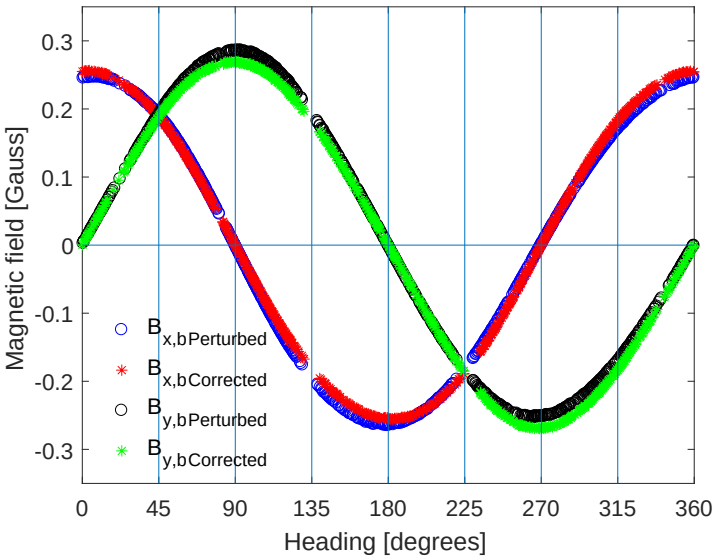

FIGURE 5.18. Comparison of heading with and without hard iron corrections during the calibration process.

.

5.3.3 Airspeed Calibration

To measure the wind speed a Pitot tube connected to an airspeed sensor is used. However Pitot tubes may lead to inaccurate results when measuring low speeds since the difference between the total and the static pressures may be too low in theses cases. The aim of the calibration process is to know the range of wind speeds for which the combination of the Pitot tube plus the digital airspeed sensor embedded in the weather station is reliable. In order to achieve this objective an open wind tunnel and a hot wire thermal anemometer were used as a reference (Figure 5.21).

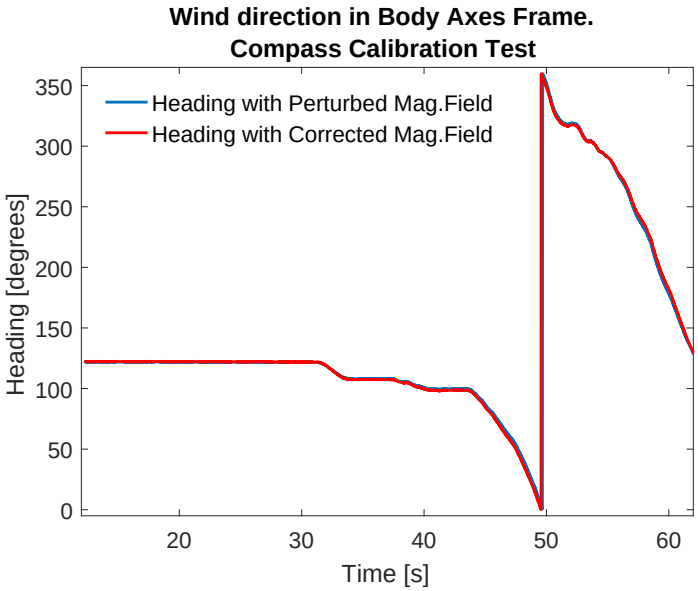

FIGURE 5.19. Wind direction during the calibration test. Body axes reference frame (clockwise direction starting from North considered as positive heading).

A thermal anemometer has a wire (Figure 5.20) which is heated at a constant temperature T_w. The amount of current needed to maintain this temperature constant when airflow crosses the wire is related to the velocity of the air. The airflow (which is at temperature T_f) crosses the wire producing fluctuations in its resistance (R_w) since these parameters are related as follows [11]:

$$I^2 R_w = h A_w (T_w - T_f) \tag{5.9}$$

where h is the heat transfer coefficient of the wire and A_w its cross sectional area. On the other hand, the resistance of the wire can be defined as:

$$R_w = R_{ref} \left[1 + \alpha (T_w - T_{ref})\right] \tag{5.10}$$

being R_{ref} the resistance of the wire at a reference temperature T_{ref}. Combining the two last equations and knowing that the heat transfer coefficient is related to the fluid velocity in the following way:

$$h = a + b V_f^c \tag{5.11}$$

V_f can be obtained. Coefficients a, b and c are obtained from calibration.

During the test the weather station was positioned in such a way that the Pitot tube was aligned with the wind coming from the tunnel [Figure 5.21(c)]. The wind tunnel airspeed was varied manually from 2 to 10 m/s and an Alnor Model AVM410 anemometer [Figure 5.21(d)] was used to measure it, taking care of positioning it perpendicular to the air stream [Figure 5.21(b)]. The instrument has the following specifications [2]:

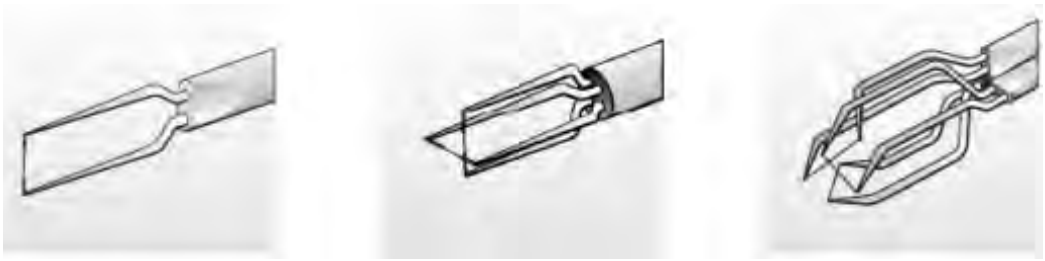

FIGURE 5.20. Different hot wires configurations. From [66].

- Airspeed range: up to 20 m/s
- Airspeed accuracy: ±5% of reading or ±0.025 m/s, whichever is greater.
- Airspeed resolution: 0.01 m/s
- Temperature range: -18 to 93 °C
- Temperature accuracy: ±0.3 °C
- Temperature resolution: 0.1 °C

Measurements were taken in intervals of one minute. The reason why this interval is large is because the wind tunnel takes time until it delivers a constant airspeed. Therefore the result given by the anemometer requires time to be stabilized. The indicated airspeed given by the anemometer during the test is gathered in Table 5.1.

Time [s]	0	60	120	180	240	300	360	420	480	540	600	660
Wind Tunnel IAS [m/s]	2.40	3.45	4.10	4.33	5.00	6.18	7.20	8.25	8.74	8.96	9.58	9.98

Table 5.1: Raw IAS data measured by the anemometer during the airspeed calibration test.

Due to its high sensitivity hot wire anemometers are appropriate to measure low speeds with high accuracy. Therefore results obtained from the wind tunnel test can be considered suitable to be used as a reference for the weather station airspeed sensor. This sensor measures the difference between static and total pressure with a pressure transducer, as it was explained in Chapter 4. The specifications of the pressure transducer embedded in the airspeed sensor regarding its accuracy is given as: ±0.25FS (Full Scale). The Full Scale is the maximum value that the sensor can measure, in this case 1 psi or 6894.76 Pa. Therefore its accuracy in terms of pressure difference will be given by:

$$\delta p = \pm 0.0025 \times 6894.76\text{Pa} = \pm 17.24\text{Pa} \tag{5.12}$$

However what is interesting for the airspeed calibration is the precision in terms of speed. Since the airspeed is not a direct measurement in principle, the accuracy of the sensor providing

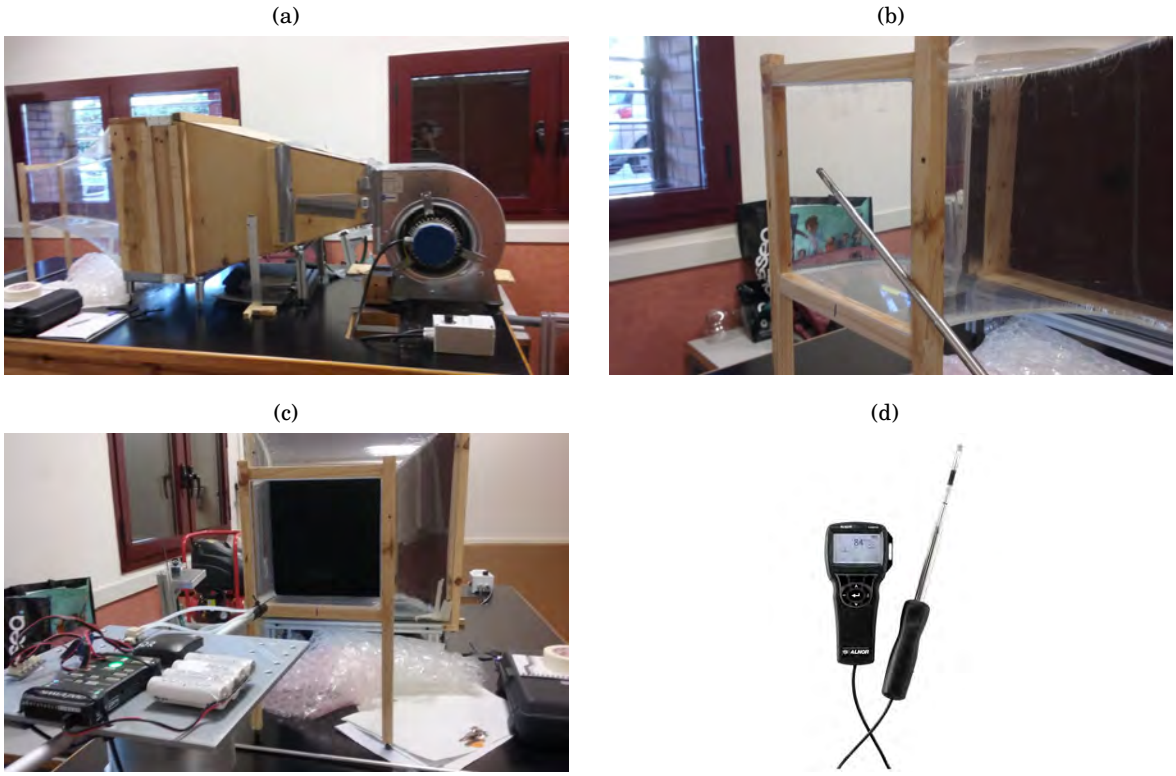

FIGURE 5.21. Airspeed calibration test in the wind tunnel (a,b,c) and anemometer used to measured the airspeed (d).

this variable should be obtained using the relation with the direct measurement (pressure difference). This relation comes from Bernoulli's equation (4.9):

$$V = \sqrt{\frac{2\Delta p}{\rho}} \tag{5.13}$$

On the other hand, the error of an indirect measurement (in this case δV) can be computed as follows:

$$\delta V = \frac{dV}{dp}\delta p \tag{5.14}$$

where dV/dp is the derivative of the indirect variable with respect to the direct one. Computing the derivative from Eq. 5.13 the previous equation turns out to be:

$$\delta V = \frac{\delta p}{\sqrt{2\rho\Delta p}} \tag{5.15}$$

It seems that the precision of the sensor in terms of airspeed is inversely proportional to the pressure difference it measures. Therefore the instrumentation error will be higher at low pressure differences and thus at low speeds, as it was expected.

Figure 5.22 shows the comparison between the indicated airspeed measured with the thermal anemometer and its corresponding instrument error given in its specifications and the same measurements given by the airspeed sensor, considering its error as the one previously calculated from the indirect procedure.

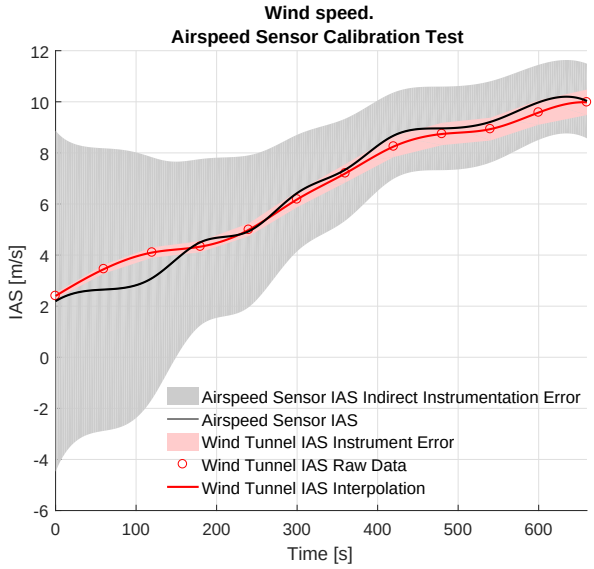

FIGURE 5.22. Airspeed calibration test results.

It can be observed that this error is extremely high leading to the conclusion that this sensor is not accurate measuring low airspeeds. However it seems that for speeds $V \geq 3.5$ m/s the measurement provided by the sensor lies within the range of speeds provided by the anemometer. Considering those values as reliable the airspeed sensor could be considered accurate enough to measure velocities from this value on.

CHAPTER 6

TESTING AND RESULTS

This chapter describes a test performed with the weather station in order to obtain the direction and magnitude of the wind velocity after setting up all the instrumentation. This results are referred to the wind at the weather station's height. A correction will be proposed with the intention of adjusting this velocity to the kite's height with a view to future flight test campaigns. Moreover the process followed to acquire the data from the Pixhawk data logger is described.

6.1 Data acquisition and processing

The Pixhawk controller logs the test data with an interval of one micro-second in a micro SD card using an app called *sdlog2* [20]. The logs are binary files which are stored in the card in *.px4log* format. In order to read the data of these files they have to be converted from binary to .csv readable format. This process has been done making use of a python script called *sdlog2dump.py* [21]. A code in Matlab was developed in order to call this function and process the data obtained from the .csv in order to compute the compass and airspeed sensor calibration parameters during the calibration tests described in Chapter 5, and to obtain the wind velocity (heading and speed).

6.2 Weather Station Test Results

After carrying out the heading and airspeed calibration tests, a final test was performed with the intention of obtaining the wind heading and speed letting the weather station to rotate freely. The test was carried out at the same location where the compass calibration test was done (see Section 5.3.2.2). Results are shown in Figure 6.1. They show the magnitude of the wind velocity

and its direction with respect to True North during an approximate interval of three minutes. It is considered that clockwise direction starting from North is a positive heading.

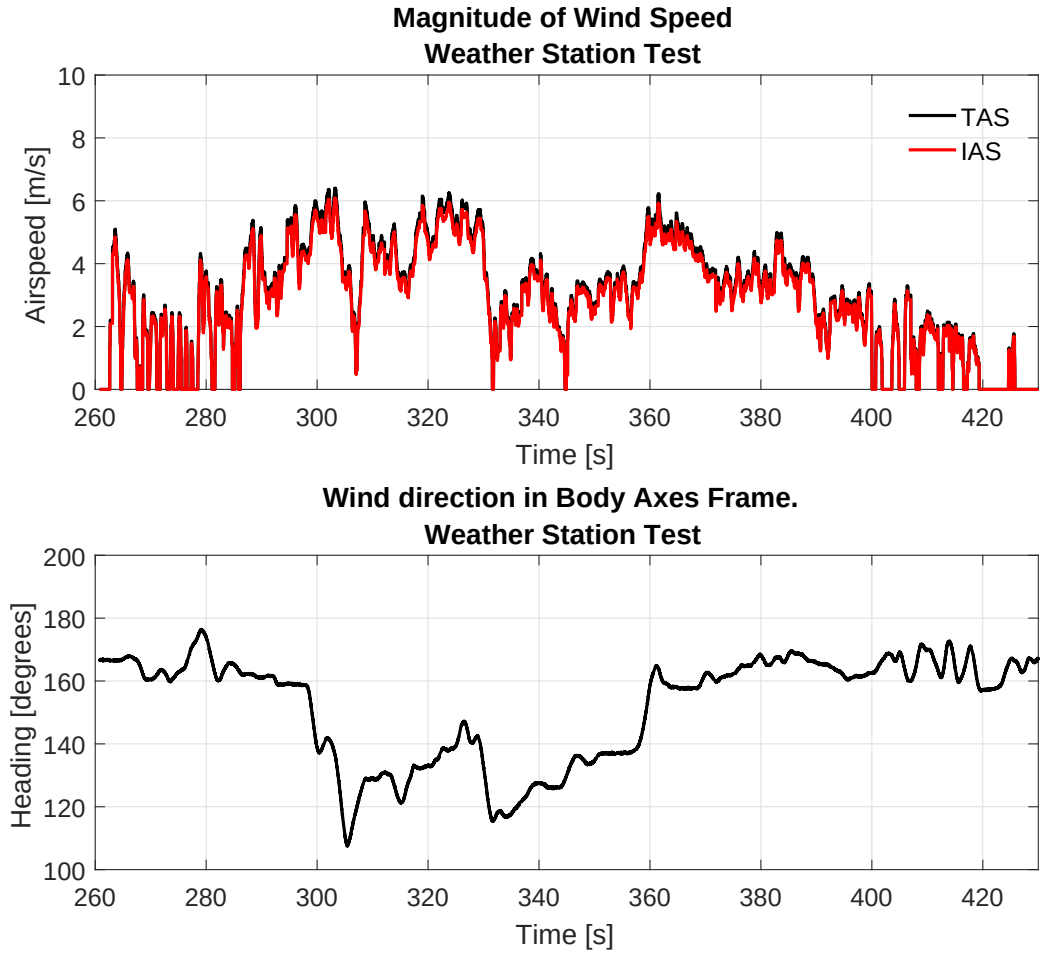

FIGURE 6.1. Wind speed and direction during the weather station test.

.

6.3 Altitude correction for future flight test campaigns

The previous results are obtained at the weather station height. However, inside the atmospheric boundary layer the wind speed magnitude changes as long as the the wind separates from the ground and the effect of friction diminishes [37]. To estimate the wind speed at the kites height $[V_w(h_{kite})]$ the following wind power equation can be applied [37]:

$$V_w(h_{kite}) = V_w(h_{station})\left(\frac{h_{kite}}{h_{station}}\right)^{\alpha} \tag{6.1}$$

where $h_{station}$ is the height of the weather station, h_{kite} the height above ground of the kite and the parameter α is a coefficient that depends on the presence of obstacles in the surrounding environment. Therefore it will depend on the place where flight test campaigns are performed. The values of this parameter are summarized in Table 6.1.

Terrain characteristics	**Coefficient α**
Smooth hard ground, calm water	0.10
Tall grass on level ground	0.15
High crops, hedges and shrubs	0.20
Wooded country side, many trees	0.25
Small town with trees and shrubs	0.30
Large city with tall buildings	0.40

Table 6.1: Values for coefficient α as a function of the terrain [37]

Future flight test campaigns are thought to be carried out in some place far from the city where kites can fly freely without encountering any obstacle. Thus the best option would be a flat vast field ($\alpha \approx 0.10$). In the worst case, a country side surrounded by trees could be chosen ($\alpha \approx 0.25$). In Figure 6.2 the wind speed from the last test has been adapted to a height of h_{kite}=25 m above ground in the different environments where the test may be performed. It has been considered that the weather station with the tripod fully extended can reach a height $h_{station}$=2 m. Looking at the results, it can be deduced that the location of the weather station will influence significantly the difference between the wind speed measured by the station and the estimation of this variable at the kites height. In order to minimize errors, smooth terrains should be chosen.

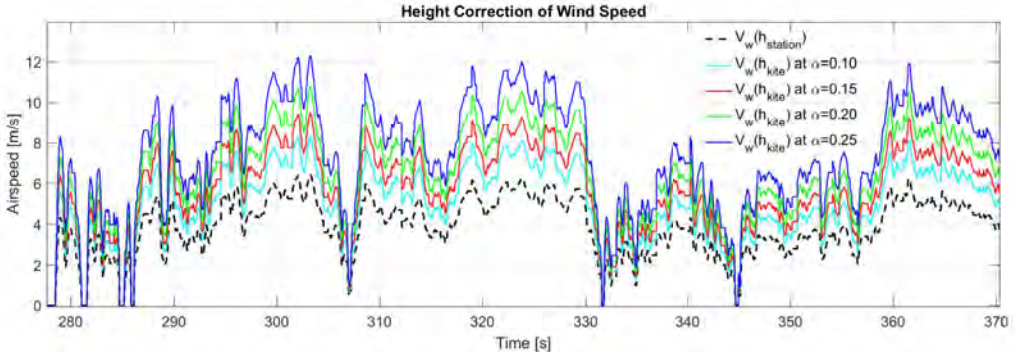

FIGURE 6.2. Wind speed height correction in different environments.

.

Regarding the heading of the wind, it can be considered unchangeable up to 50-100 m height above ground due to the effects of viscosity [71]. Considering the height range suitable for the UC3M kite-surf kites (up to 30 m), this assumption may be applied. Thus no corrections in the wind direction will be taken into account.

CHAPTER 7

CONCLUSIONS AND FUTURE WORK

The main goal of this thesis was to give some light in the Airborne Wind Energy research that is being conducted at UC3M. From the work done during the project, it can be concluded that:

- Two kite-surf kites that will be used in future experimental test have been characterized using a CAD software. Results support the use of semi-elliptical models in the Matlab simulator as an estimation. However the improvement of the model towards a more realistic shape could be recommended if more accurate results are desired. On the other hand, it has to be taken into account that the dimensions and weight of the kites were obtained manually, with the aid of a measuring tape and a scale (the tools that were available at the university). These instruments introduce some errors in the measurements and therefore in the CAD models. To give an estimation this procedure seems to be fairly enough. However, if more accurate results are desired more precise tools should be used to characterize the kites.

- A weather station able to obtain the wind speed and heading has been designed taking into account several requirements. The system is the result of combining a tripod, a very sensitive bearing, 3D impression and some instrumentation: a Pitot tube connected to an airspeed sensor to measure wind speed, a magnetometer to determine wind direction and a Pixhawk controller to log all data. The weather station seems to be sensitive to a minimum speed of 0.06 m/s, and can be used in any kind of terrain. Moreover, it has been designed to be compatible with the instrumentation on board the kites.

- The use of a magnetometer to obtain the wind heading seems to be appropriate. The compass has been calibrated making an estimation of the perturbations that the components of the

weather station may introduce in the magnetic field. Results show that these disturbances are mostly of hard-iron type and small enough to not perturb the computation of the heading. Therefore, it was decided that they could be neglected assuming that the only error in the measurements comes from the instrumentation error of the magnetometer itself: 1°-2°, according to its specifications.

- On the other hand, the combination of a Pitot tube and an airspeed sensor with a pressure transducer provides reliable results at high speeds. However it seems not to be the best option to obtain low speeds, specially below 3.5 m/s. Apparently, the indirect error that the airspeed sensor commits providing the airspeed is huge, although it is accurate enough computing the pressure difference. It has to be mentioned that this sensor was used first because the research group at the university had it already and it was not selected specifically for this project. Considering the results after calibration, it is recommended that the research group comes to the decision on which sensor it will use in the future. Maybe for the typical height the kites will fly at (winds no more than 10-15m/s), the sensor should be changed. Anyway, the results from the airspeed calibration test should not be taken as definitive since measurements were taken just once. In order to be reliable, experiments should be done over.

- The results given by the weather station are referred to the height at which the sensors are located (approximately 2 m above ground). However, wind speed increases with height thus a correction was made with the intention of adapting the velocity magnitude at the kites height. Results demonstrate that this correction is proportional to the amount of perturbations in the surrounding environment. The smoother the terrain the more reliable the speed obtained by the station is. Therefore the selection of the environment is key for future test campaigns. On the other hand, the wind direction seems not to need any correction since, according to the specified references, it remains unchangeable up to heights of 50-100 m.

7.1 Future Work

Although this project has covered the main objectives proposed at the beginning, there are some aspects that could be further improved and others that may be accomplished using the results presented in this thesis. Some ideas that are interesting to work on in the future are:

- To repeat the airspeed calibration test in the wind tunnel. During this project and due to technical reasons only one test could be carried out. It would be needed to repeat the experiment several times with the intention of obtaining more reliable results introducing a statistic error, besides the instrumentation one.

- To look for alternatives in the way of measuring the airspeed magnitude with more accuracy at low speeds. Maybe an anemometer with higher precision can be adapted to the weather station. However special attention should be paid to the way of coordinating it with the sensors on-board the kites.
- To do a flight test campaign combining the kites and the weather station. During this campaign the ground velocity of the kites should be obtained from data provided by the Pixhawk on-board. Simultaneously the wind velocity given by the weather station should be obtained.
- To compute the aerodynamic velocity of the kites using the data provided during the flight test campaign. It should be quite straight forward to be calculated taking into account the compatibility among the sensors. Both Pixhawk log data with the same time interval thus allowing to compute the aerodynamic velocity of the kites without the need of any time adaptation.
- To use the data obtained from the kites characterization in the Matlab simulator. And to combine them with experimental data from flight tests in order to characterize the aerodynamic coefficients of the kites.

These previous concerns are the ones that have emerged after carrying out this specific project. However due to the experimental nature of this research, it is likely that further considerations regarding its development may arise in the near future.

APPENDIX A

DIMENSIONS OF THE CAD MODELS

Here are the dimensions in mm of the CAD models used in the project. First of all, the dimensions of both kites are shown in Figures A.1 and A.2. Measurements were taken manually and applied to both CAD models. On the other hand, dimensions of the weather station elements which have been designed with the aid of 3D printing are shown in Figures A.3 - A.6.

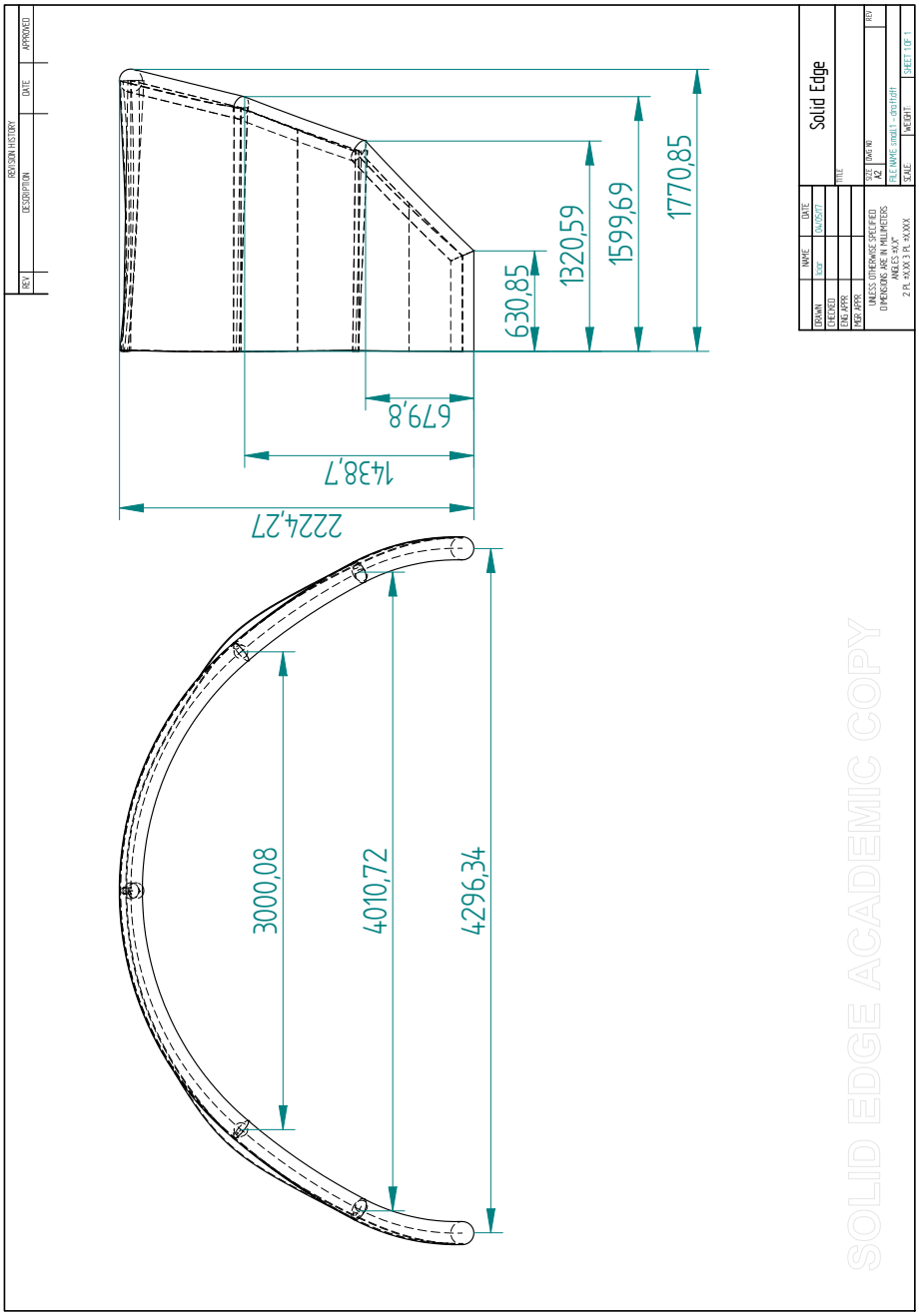

FIGURE A.1. Small kite dimensions

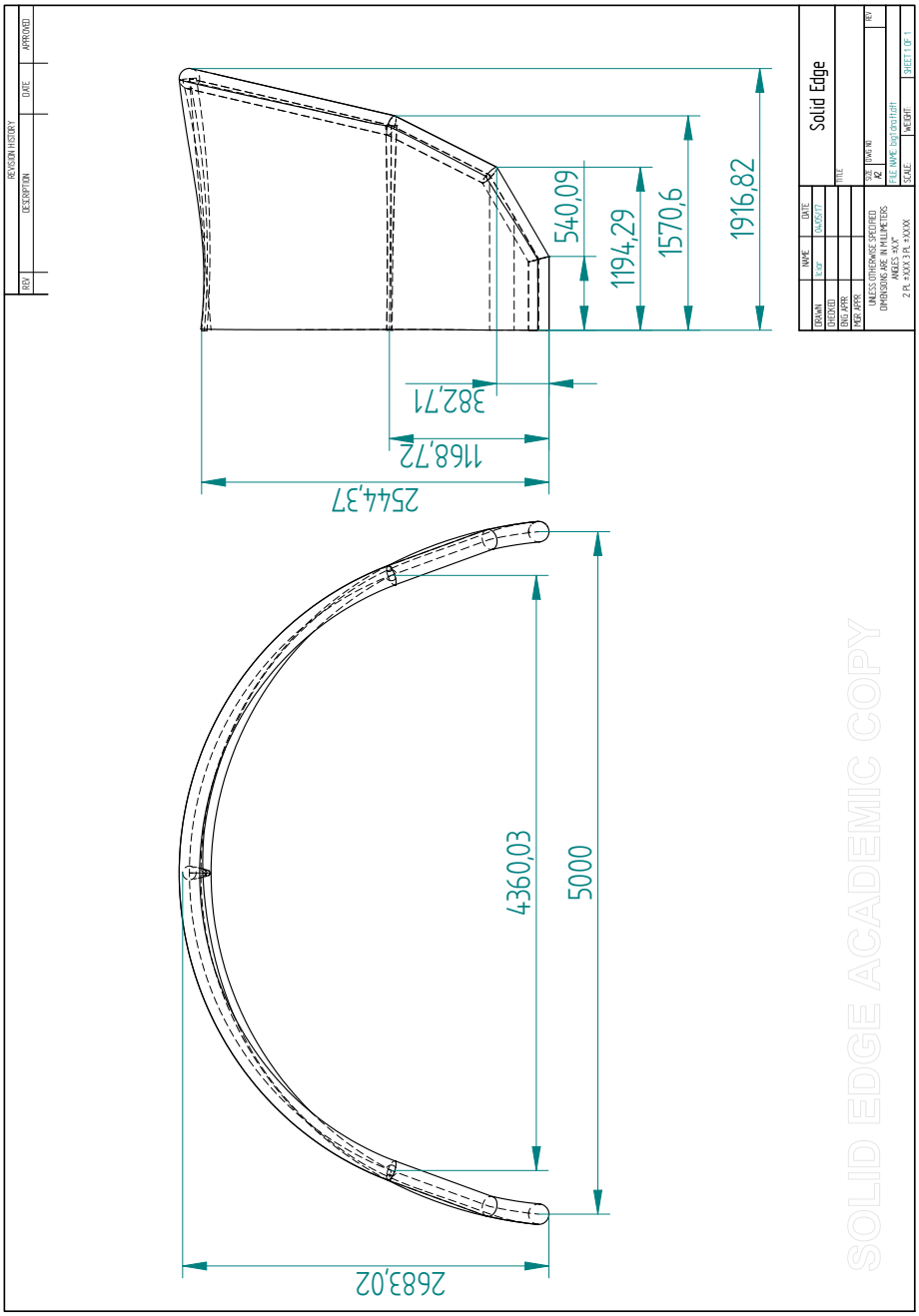

FIGURE A.2. Big kite dimensions

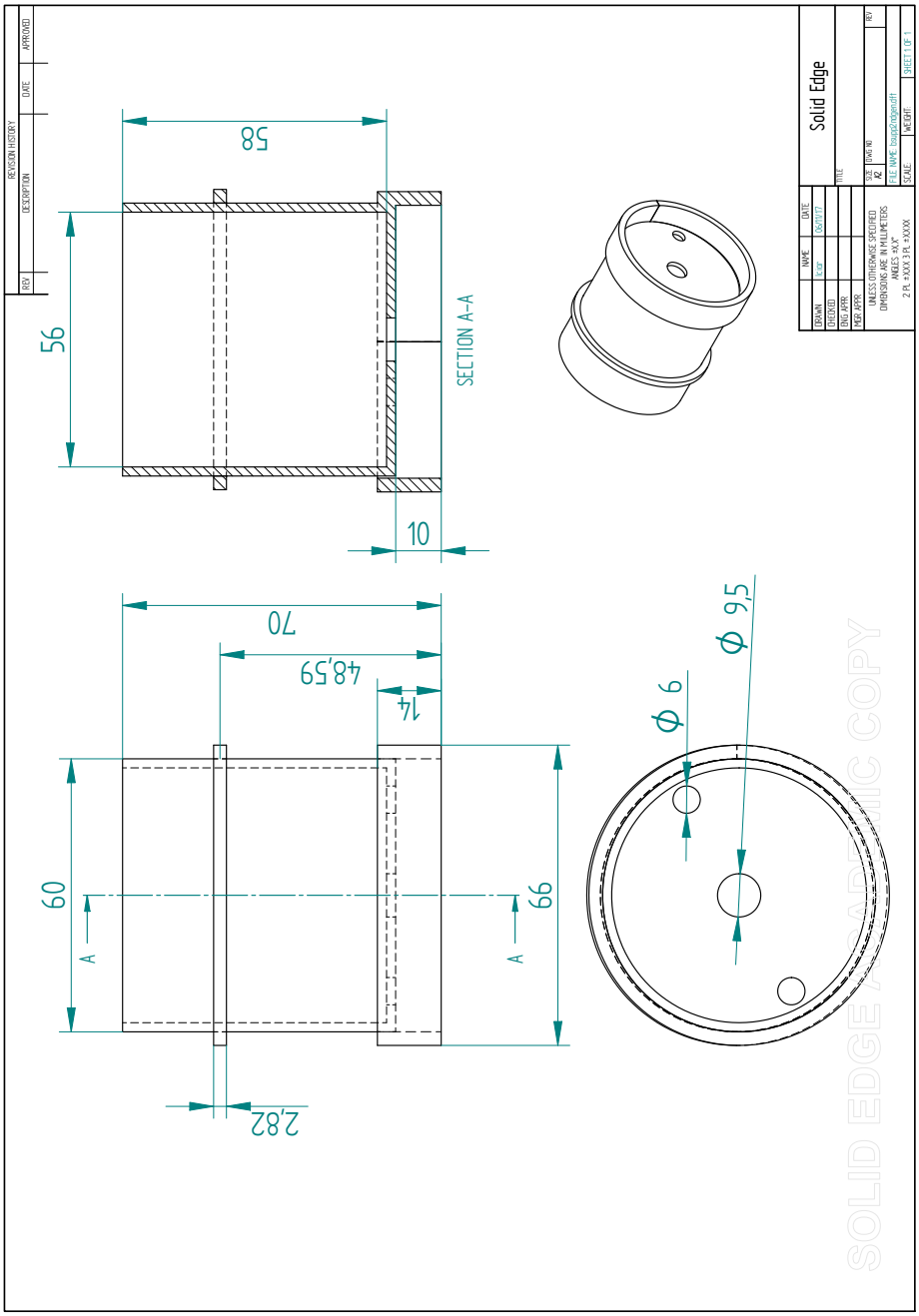

FIGURE A.3. Tripod link dimensions

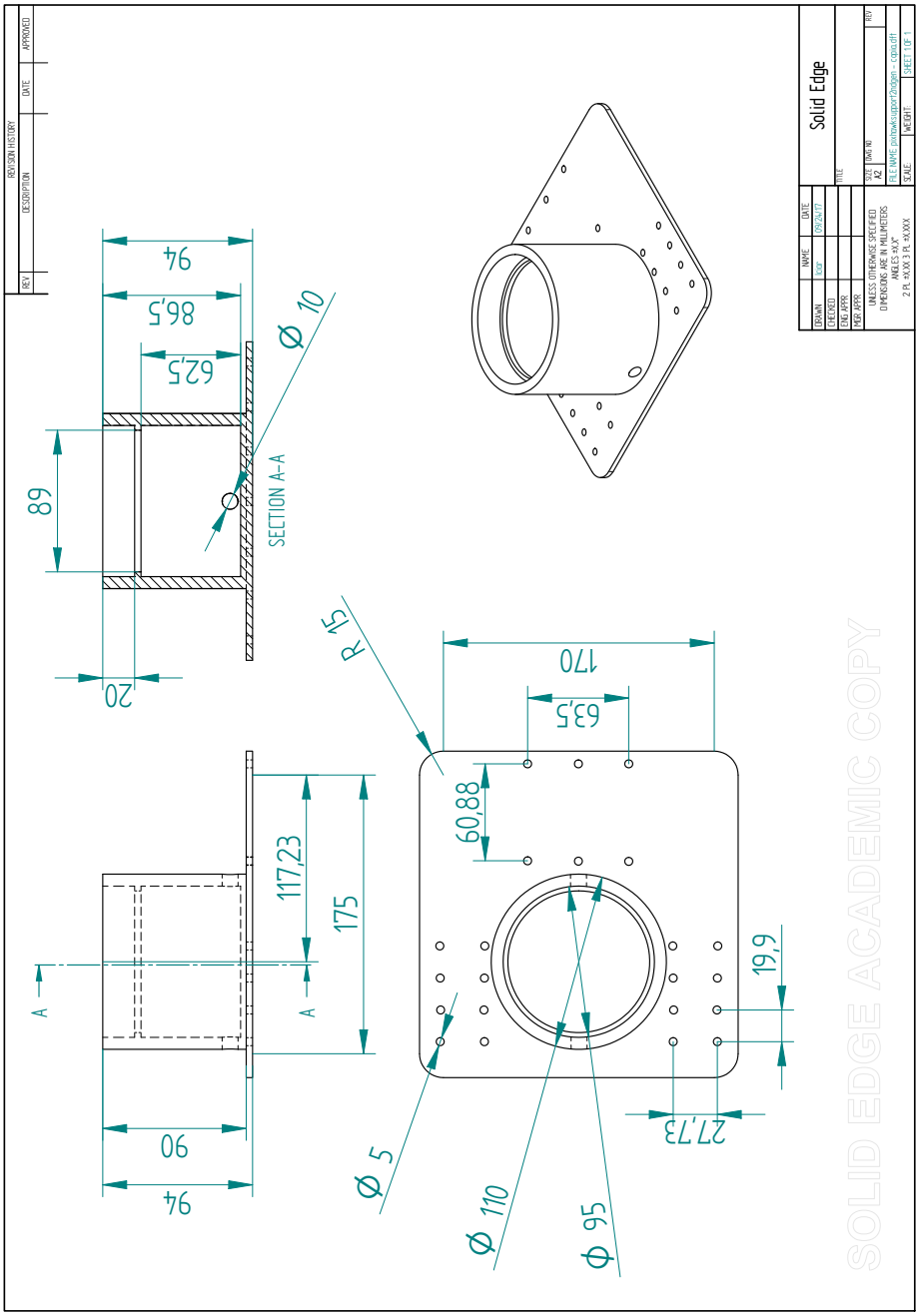

FIGURE A.4. Weather station head dimensions

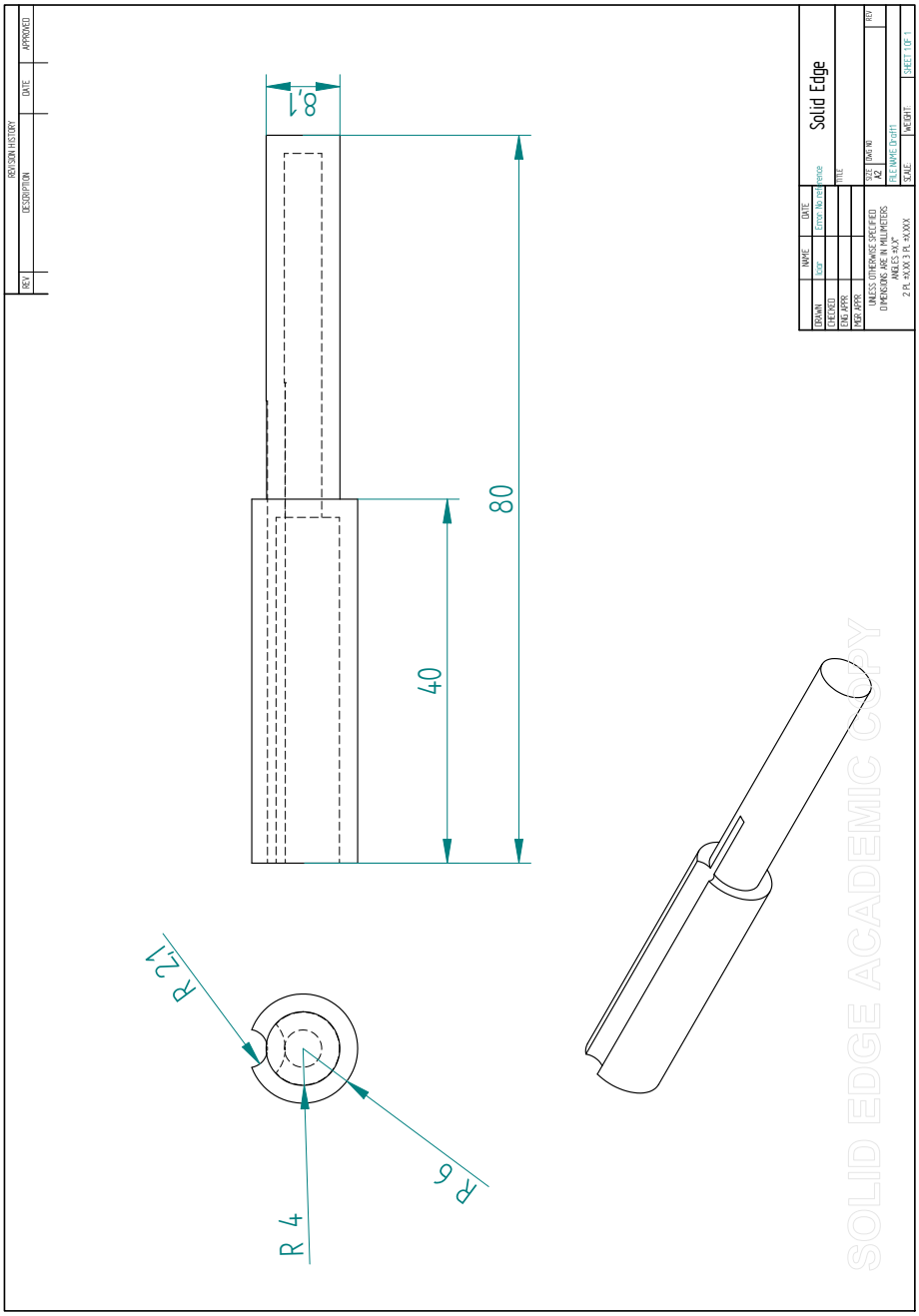

FIGURE A.5. Dimensions of the Pitot holder

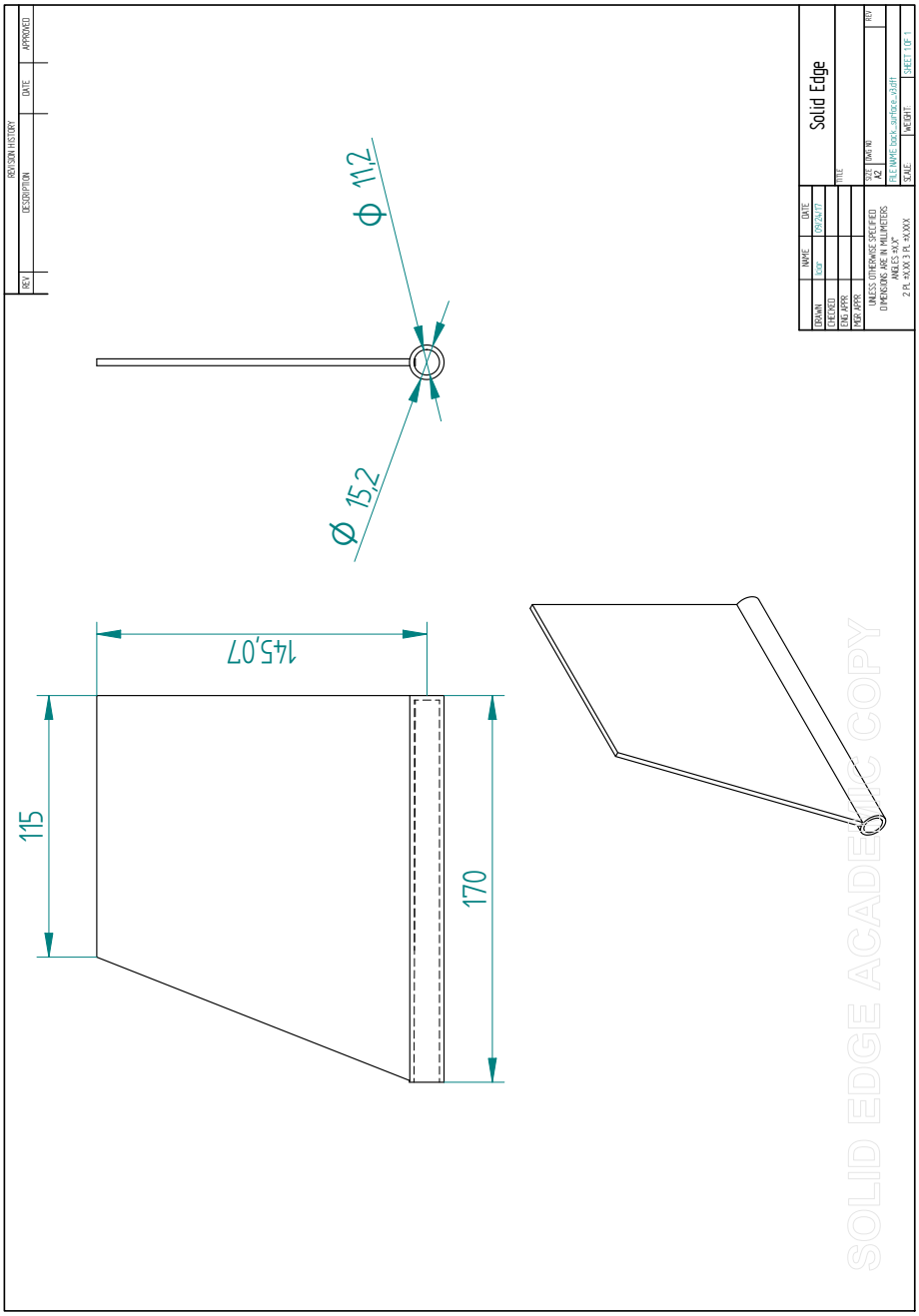

FIGURE A.6. Dimensions of the tail surface

BIBLIOGRAPHY

[1] *3-axis digital compass IC HMC5883l datasheet*.
https://cdn-shop.adafruit.com/datasheets/HMC5883L_3-Axis_Digital_Compass_IC.pdf.

[2] *Air velocity meter Alnor model AVM410 datasheet*.
http://www.tsi.com/uploadedFiles/_Site_Root/Products/Literature/Manuals/AVM410-TA410-1980575-web.pdf.

[3] *Airborne wind energy conference 2015*.
http://www.awec2015.com/.

[4] *Altaeros energies*.
http://www.altaerosenergies.com/.

[5] *Ampyx power*.
https://www.ampyxpower.com/.

[6] *Compass heading using magnetometers*.
https://aerocontent.honeywell.com/aero/common/documents/myaerospacecatalog-documents/Defense_Brochures-documents/Magnetic_Literature_Application_notes-documents/AN203_Compass_Heading_Using_Magnetometers.pdf.

[7] *Cura software*.
https://ultimaker.com/en/products/cura-software.

[8] *EIA projects world energy consumption will increase 56% by 2040*, U.S Energy Information Administration.
https://www.eia.gov/todayinenergy/detail.php?id=12251.

[9] *Enerkite*.
http://www.enerkite.de/en/products.

[10] *Hard-iron and soft-iron calibration*.
https://dkc1.digikey.com/US/en/TOD/Honeywell/Hard-Soft-Iron-Calibration/Hard-Soft-Iron-Calibration.html.

[11] *Hot-wire anemometry*.
http://www.ae.utexas.edu/courses/ase463q/design_pages/spring03/active_wing/ATAK%20Technologies%20Website/Final%20Report/Final%20Appendix%20C.pdf.

[12] *Kitegen carousel*.
http://www.kitegen.com/en/products/kite-gen-carousel/.

[13] *Magnetic declination*.
http://www.magnetic-declination.com/.

[14] *The magnetic field of the earth*, MIT.
http://www-gpsg.mit.edu/12.201_12.501/BOOK/chapter3.pdf.

[15] *Makani*.
https://x.company/makani/.

[16] *MS4525DO datasheet*.
http://www.mouser.com/ds/2/418/NG_DS_MS4525DO_B2-1130293.pdf.

[17] *NTS X-wind*.
https://www.x-wind.de/en/.

[18] *Omnidea high altitude wind energy*.
http://www.omnidea.net/hawe/concept.html.

[19] *Qgroundcontrol*.
http://qgroundcontrol.com/#resources.

[20] *sdlog2*.
https://pixhawk.org/firmware/apps/sdlog2.

[21] *sdlog2dump.py*.
https://github.com/weiweikong/px4log_to_matlab/blob/master/sdlog2_dump.py.

[22] *Shape effects on drag*, NASA.
https://www.grc.nasa.gov/www/k-12/airplane/shaped.html.

[23] *SKF rolling bearings catalogue*.
http://www.skf.com/binary/77-121486/SKF-rolling-bearings-catalogue.pdf.

[24] *Skysails power*.
http://www.skysails.info/english/company/.

[25] *Twingtec*.
http://twingtec.ch/.

[26] *Ultimaker*.
https://ultimaker.com/en/products.

[27] *Vanguard tripode auctus plus 283AT*.
http://www.fotovega.com/vanguard-auctus-plus-283at.

[28] *The world counts*.
http://www.theworldcounts.com/counters/shocking_environmental_facts_and_statistics/what_is_the_environmental_footprint.

[29] *wrldmagm.m*.
https://es.mathworks.com/help/aerotbx/ug/wrldmagm.html.

[30] *NTS X-wind. How we produce energy with large kites.*, Ahrens, Uwe., (2014).
https://www.slideshare.net/ntsXwind/nts-xwind-wow-we-produce-energy-with-large-kites.

[31] *Transposition of amendment 43 to annex 2 to the chicago convention on remotely piloted aircraft systems into common rules of the air.*, EASA, (2014).
https://www.easa.europa.eu/system/files/dfu/NPA%202014-09.pdf.

[32] *Disposicion 961 del BOE Num. 25 de 2017. Ministerio de Empleo y Seguridad Social*, 2017.
https://www.boe.es/boe/dias/2017/01/30/pdfs/BOE-A-2017-961.pdf.

[33] *Global climate change. Vital signs of the planet. Global temperature*, NASA, (2017).
https://climate.nasa.gov/vital-signs/global-temperature/.

[34] *Global climate change. Vital signs of the planet. Sea level*, NASA, (2017).
https://climate.nasa.gov/vital-signs/sea-level/.

[35] M. H. Afzal, V. Renaudin, and G. Lachapelle, *Use of Earth's magnetic field for mitigating gyroscope errors regardless of magnetic perturbation*, Sensors, 11 (2011), pp. 11390–11414.

[36] U. Ahrens, M. Diehl, and R. Schmehl, *Airborne wind energy*, Springer Science & Business Media, 2013.

[37] C. L. Archer, *An introduction to meteorology for airborne wind energy*, in Airborne wind energy, Springer, 2013, pp. 81–94.

[38] C. L. Archer and K. Caldeira, *Global assessment of high-altitude wind power*, Energies, 2 (2009), pp. 307–319.

[39] C. L. Archer, L. Delle Monache, and D. L. Rife, *Airborne wind energy: Optimal locations and variability*, Renewable Energy, 64 (2014), pp. 180–186.

[40] C. L. ARCHER AND M. Z. JACOBSON, *Evaluation of global wind power*, Journal of Geophysical Research: Atmospheres, 110 (2005).

[41] *Supplying base-load power and reducing transmission requirements by interconnecting wind farms*, Journal of Applied Meteorology and Climatology, 46 (2007), pp. 1701–1717.

[42] E. BECATOROS, *More than 90 percent of world's coral reefs will die by 2050*, Independent.co.uk, (2017).
http://www.independent.co.uk/environment/environment-90-percent-coral-reefs-die-2050-
html.

[43] J. C. BREUER AND R. H. LUCHSINGER, *Inflatable kites using the concept of tensairity*, Aerospace Science and Technology, 14 (2010), pp. 557–563.

[44] A. CHERUBINI, A. PAPINI, R. VERTECHY, AND M. FONTANA, *Airborne wind energy systems: A review of the technologies*, Renewable and Sustainable Energy Reviews, 51 (2015), pp. 1461–1476.

[45] J. CHU, *Short-lived greenhouse gases cause centuries of sea-level rise*, NASA Global Climate Change, (2017).
https://climate.nasa.gov/news/2533/short-lived-greenhouse-gases-cause-centuries-of-se

[46] W. E. COUNCIL, *World energy resources*, 2016.
https://www.worldenergy.org/wp-content/uploads/2016/10/
World-Energy-Resources-Full-report-2016.10.03.pdf.

[47] M. DIEHL, *Airborne wind energy: Basic concepts and physical foundations*, in Airborne wind energy, Springer, 2013, pp. 3–22.

[48] M. . DOE, *How to introduce kite-based airborne wind energy systems - The selection of niche strategies to overcome barriers to adoption.*, Airborne Wind Energy Conference 2015, (2015).
https://collegerama.tudelft.nl/Mediasite/Play/d923a66b221b4117872189e7a73d29e71d.

[49] B. DUDLEY ET AL., *BP statistical review of world energy 2017*, 2017.
https://www.bp.com/content/dam/bp/en/corporate/pdf/energy-economics/
statistical-review-2017/bp-statistical-review-of-world-energy-2017-full-report.
pdf.

[50] F. FRITZ, *Application of an automated kite system for ship propulsion and power generation*, in Airborne wind energy, Springer, 2013, pp. 359–372.

[51] D. GEBRE-EGZIABHER, G. H. ELKAIM, J. DAVID POWELL, AND B. W. PARKINSON, *Calibration of strapdown magnetometers in magnetic field domain*, Journal of Aerospace Engineering, 19 (2006), pp. 87–102.

[52] L. GROZDANIC, *World's first airborne wind turbine to bring renewable energy and wifi to Alaska*, Inhabitat.com, (2014).
http://inhabitat.com/worlds-first-airborne-wind-turbine-to-bring-renewable-energy-and-wifi buoyant-airborne-turbine-altaeros-energies-3.

[53] J. HILARIO, *Generalities and operating environment*, in Class notes for Aircraft Design, Universidad Carlos III de Madrid, Spain, 2017.

[54] M. Z. JACOBSON AND C. L. ARCHER, *Saturation wind power potential and its implications for wind energy*, Proceedings of the National Academy of Sciences, 109 (2012), pp. 15679–15684.

[55] J. MAASS AND M. ERHARD, *Software system architecture for control of tethered kites*, in Airborne wind energy, Springer, 2013, pp. 599–611.

[56] MAKANI, *Makani energy kite*.
https://www.youtube.com/watch?v=GSYMHzgLLn8.

[57] *Makani's first commercial-scale energy kite*.
https://www.youtube.com/watch?v=An8vtD1FDqs.

[58] K. MARVEL, B. KRAVITZ, AND K. CALDEIRA, *Geophysical limits to global wind power*, Nature Climate Change, 3 (2013), pp. 118–121.

[59] M. MILANDRI, *Design of a kite controller for airborne wind energy*, PhD thesis, University of Cape Town, 2015.

[60] NASA, *Pitot-static tube*.
https://www.grc.nasa.gov/www/k-12/airplane/pitot.html.

[61] T. I. C. ON SYSTEMS ENGINEERING (INCOSE), *What is systems engineering?*, 2017.
http://www.incose.org/AboutSE/WhatIsSE.

[62] S. ROHRINGER, *Pla vs abs: Filaments for 3d printing explained and compared*, All3dp.com, (2017).
https://all3dp.com/pla-abs-3d-printer-filaments-compared/.

[63] R. RUITERKAMP, *Update on certification and regulations of airborne wind energy systems. European case of rigid wings*, Airborne Wind Energy Conference 2015, (2015).
https://collegerama.tudelft.nl/Mediasite/Play/c8a9806aea024394a36cc35f9d6e98a81d.

[64] R. RUITERKAMP AND S. SIEBERLING, *Description and preliminary test results of a six degrees of freedom rigid wing pumping system*, in Airborne wind energy, Springer, 2013, pp. 443–458.

[65] G. SÁNCHEZ-ARRIAGA, M. GARCIA-VILLALBA, AND R. SCHMEHL, *Modeling and dynamics of a two-line kite*, Applied Mathematical Modelling, 47 (2017), pp. 473–486.

[66] R. P. SANGRAM, *Hot-wire anemometry and fluid flow measurements*, in Class notes for Fluid Mechanics and Heat Transfer, IIT Bombay, India, 2017.
http://www.leb.eei.uni-erlangen.de/winterakademie/2009/report/content/course01/pdf/0106.pdf.

[67] A. SERINO, *On-board instruments and flight tests of giant kites applied to wind power generation*, Universidad Carlos III de Madrid and Politecnico di Torino, (2016).

[68] F. STEVENS, M. MONROE, AND L. DI CAPRIO, *Before the flood (documentary)*.

[69] M. TRIMARCHI, *How much power does the world consume?*, HowStuffWorks.com.
http://science.howstuffworks.com/environmental/green-science/world-power-consumption.htm.

[70] C. VERMILLION, B. GLASS, AND A. REIN, *Lighter-than-air wind energy systems*, in Airborne Wind Energy, Springer, 2013, pp. 501–514.

[71] X. ZHENG, *Mechanics of wind-blown sand movements*, Springer Science & Business Media, 2009.

[72] U. ZILLMANN AND S. HACH, *Financing strategies for airborne wind energy*, in Airborne Wind Energy, Springer, 2013, pp. 117–137.